ACS chemical biology

pubs.acs.org/acschemicalbiology

Articles

Discovery of All-D-Peptide Inhibitors of SARS-CoV-2 3C-like Protease

Raphael J. Eberle, Marc Sevenich, Ian Gering, Lara Scharbert, Birgit Strodel, Nils A. Lakomek, Karoline Santur, Jeannine Mohrlüder, Mônika A. Coronado,* and Dieter Willbold*

Cite This: *ACS Chem. Biol.* 2023, 18, 315−330

Read Online

ACCESS | Metrics & More | Article Recommendations | Supporting Information

ABSTRACT: During the replication process of SARS-CoV-2, the main protease of the virus [3-chymotrypsin-like protease (3CL^{pro})] plays a pivotal role and is essential for the life cycle of the pathogen. Numerous studies have been conducted so far, which have confirmed 3CL^{pro} as an attractive drug target to combat COVID-19. We describe a novel and efficient next-generation sequencing (NGS) supported phage display selection strategy for the identification of a set of SARS-CoV-2 3CL^{pro} targeting peptide ligands that inhibit the 3CL protease, in a competitive or noncompetitive mode, in the low μM range. From the most efficient L-peptides obtained from the phage display, we designed all-D-peptides based on the retro-inverso (ri) principle. They had IC_{50} values also in the low μM range and in combination, even in the sub-micromolar range. Additionally, the combination with Rutinprivir decreases 10-fold the IC_{50} value of the competitive inhibitor. The inhibition modes of these D-ri peptides were the same as their respective L-peptide versions. Our results demonstrate that retro-inverso obtained all-D-peptides interact with high affinity and inhibit the SARS-CoV-2 3CL protease, thus reinforcing their potential for further development toward therapeutic agents. The here described D-ri peptides address limitations associated with current L-peptide inhibitors and are promising lead compounds. Further optimization regarding pharmacokinetic properties will allow the development of even more potent D-peptides to be used for the prevention and treatment of COVID-19.

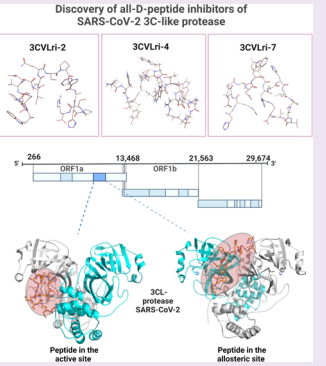

1. INTRODUCTION

The spread of Coronavirus disease 2019 (COVID-19) caused by severe acute respiratory syndrome coronavirus 2 (SARS-CoV-2), with increasing levels of infectivity and transmissibility, has strained human health and public safety worldwide.[1] By May 2022, the COVID-19 pandemic has resulted in more than 524 million confirmed cases and more than 6.2 million confirmed deaths, according to the World Health Organization (WHO).[2] To date, vaccination is considered the key strategy for ending the pandemic[3] and the worldwide vaccination campaign using clinical safe and efficient vaccines against SARS-CoV-2 have controlled the number of death. However, not yet the spread of the diseases.[4−7] So far, more than 11.8 billion vaccine doses have been administered.[2] Remdesivir, Dexamethasone, Favipiravir, Lopinavir/Ritonavir, Nirmatrelvir/Ritonavir (Main protease inhibitor), and Darunavir have been approved for emergency use to inhibit SARS-CoV-2 infection and replication.[8−12] Given a considerable limitation of direct-acting antivirals for COVID-19 and an increasing presence of SARS-CoV-2 variants (B.1.1.529, B.1.617.2, B.1.1.7, B.1.351, A.23.1, B.1.525, B.1.526 and P.1),[13] it remains a strategic priority to develop new drug candidates with minimal side effects and also targeting the new variants.

For the expression and replication of the CoV gene, proteases play essential roles involving the proteolytic processing of replicase polyproteins, which makes them attractive targets for drug development.[14,15] The main protease, also called 3CL protease (3CL^{pro}), is the 3-chymotrypsin-like cysteine protease that features a His41-Cys145 catalytic dyad. A glutamine (Gln) residue is commonly located at the P1 site on the protease substrate. No known human cysteine protease cleaves after Gln, thus offering potential selectivity for this viral target over human proteases.[16,17] Viral proteases have been attractive targets for oral small-molecule therapies in treating HIV and HCV.[18,19] The use of SARS-CoV-2 3CL^{pro} as a drug target has several advantages over other virus proteins: (i) its essential role in the viral replication process, (ii) its potential for mechanistic safety, and (iii) the expected lack of variant resistance challenges.[8] 3CL^{pro} inhibition represents an attractive approach for a safe and orally available antiviral therapy to treat COVID-19.

Drugs are conventionally classified into two molecule weight classes: "small-molecule" drugs (<500 Da) and protein/peptide-based drugs (>1000 Da).[20] Besides the obvious advantages of small molecules like favorable oral bioavailability and a rational design,[21] they often have low target selectivity, ultimately resulting in side effects. In comparison, peptides were often neglected as potential molecules for drug development, despite binding to their target proteins with high affinity and specificity. They are smaller than proteins and can be obtained synthetically

Received: September 22, 2022
Accepted: December 1, 2022
Published: January 17, 2023

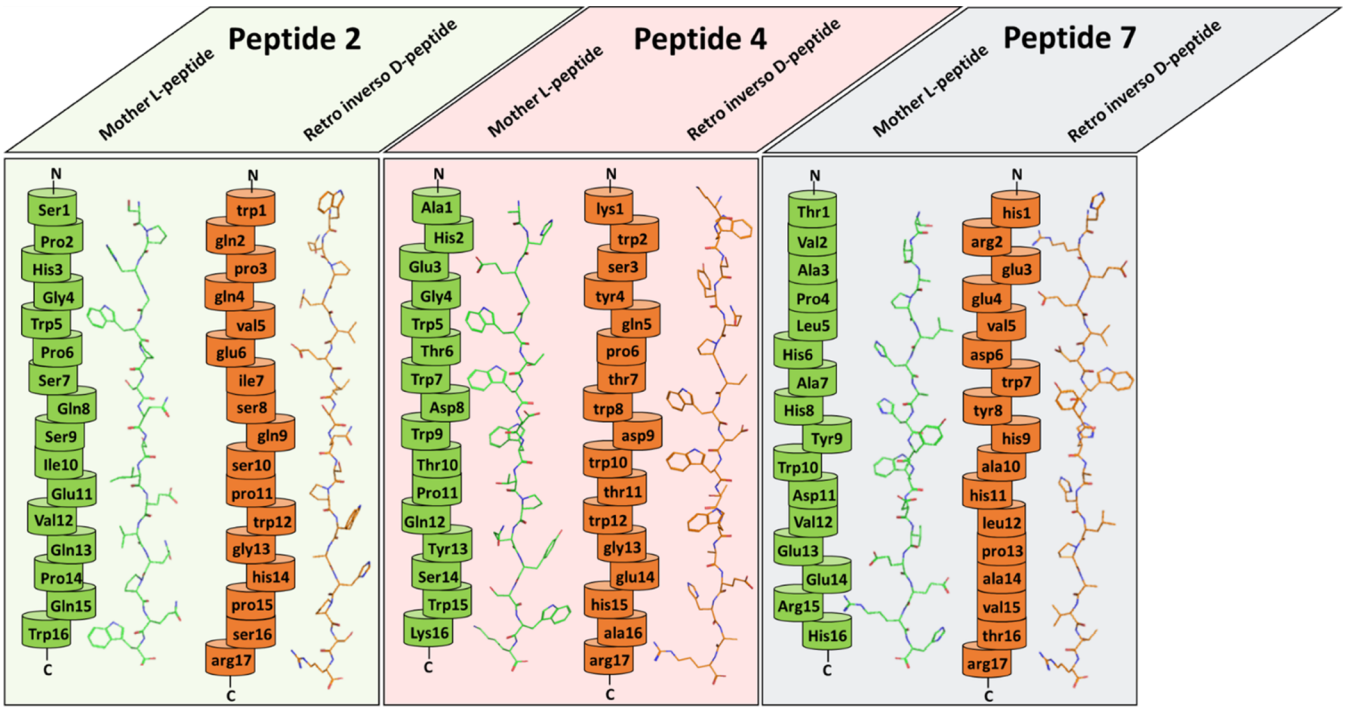

Figure 1. Schematic overview of the investigated D-ri peptides and their mother L-peptides.

by well-established and cost-efficient methods.[22] The disadvantages of peptide drugs are their potential immunogenicity and low bioavailability due to degradation and short half-lives. Several approaches have been developed to approach these problems. D-Enantiomeric amino acid residues effectively enhance the resistance to degradation since most proteolytic enzymes have substrate specificity for L-peptide bonds, allowing oral administration of D-enantiomeric peptides.[23,24] Furthermore, all-D-peptides are less immunogenic.[25]

Several studies described the development of the first all-D-peptide designed to treat Alzheimer's disease, and it proved to be efficient in animal models and safe in humans.[26−28] In the case of SARS-CoV-2, several studies describe the identification of D-peptide inhibitors against SARS-CoV-2 Spike protein and $3CL^{pro}$.[29−32] Of particular interest are all-D-peptides composed of D-amino acid residues. However, many peptide-based drug development strategies, like phage display selection, end up with L-peptides. So-called D-retro-inverso (D-ri) peptides are composed solely of D-amino acid residues in the reverse sequence of their parental L-peptide (Figure 1). Such a peptide assembled in reversed sequence from D-amino acid residues will have almost the same structure, stability, and bioactivity as its parent peptide made of L-amino acid residues, but with the advantage of being more resistant to proteolytic degradation. This combination makes D-ri peptides attractive drug candidates.[33] The overall orientation of the side chains of the D-ri peptides is very similar to the original L-peptides, which, however, does not lead to perfect D-ri peptides, which is undoubtedly one reason why the retro-inverso approach was not successful in every case.[34−36]

However, in this paper, we demonstrate the inhibition potential of L-peptides selected using phage display targeting SARS-CoV-2 $3CL^{pro}$. Subsequently, its retro-inverso versions were explored, also in combination.

2. RESULTS

2.1. Characterization of SARS-CoV-2 $3CL^{pro}$ Inhibition by L- and D-Retro-Inverso Peptides. All experiments were performed with recombinant produced SARS-CoV-2 $3CL^{pro}$ protein (Supporting Information, Figure S1). To select binding L-peptides to the $3CL^{pro}$, M13 phage display selection was performed (Figure 2A). Detailed information about the phage display process is described in Supporting Information, Text S1, Figures S2 and S3, and Tables S1−S3. To verify whether the selected peptides showed inhibition toward the target protein, they were primary tested using a final concentration of 10 μM of each peptide, separately, in an enzyme-based fluorescence assay (Figure 2B). With more than 60% inhibition, the peptides 3CVL-2 (SPHGWPSQSIEVQPQW), 3CVL-4 (AHEGWTWDWTPQYSWK), and 3CVL-7 (TVAPLHAHYWDVEERH) were selected for further analysis (Figure 2C−E). Concerning their potential to inhibit 100% of the protease activity, determination of the IC_{50} was performed using 0−140 μM (3CVL-2), 0−120 μM (3CVL-4), and 0−100 (3CVL-7). The 3CVL-2 at a final concentration of 140 μM showed 100% inhibition of the protease (Supporting Information, Figure S4A) with a calculated IC_{50} value of 4.90 ± 0.8 μM (Table 1 and Figure 2C). In a similar concentration range, the tested 3CVL-4 inhibited 100% of the protease activity at a final concentration of 120 μM (Supporting Information, Figure S4C), presenting an IC_{50} value of 2.44 ± 0.6 μM (Table 1 and Figure 2D). The selected peptide 3CVL-7 performs even better and inhibits 100% of the recombinant SARS-CoV-2 protease activity at a final concentration of 80 μM (Supporting Information, Figure S4E) with an IC_{50} value of 0.98 ± 0.2 μM (Table 1 and Figure 2E). Further inhibition mode assays identified 3CVL-2 and 3CVL-7 as competitive inhibitors. These peptides compete with the substrate for the active and/or binding sites of the protease (Supporting Information, Figure S4B,F). Remarkably, the inhibition mode has shown that $3CL^{pro}$ can be allosterically inhibited by 3CVL-4, which discloses a

https://doi.org/10.1021/acschembio.2c00735
ACS Chem. Biol. 2023, 18, 315−330

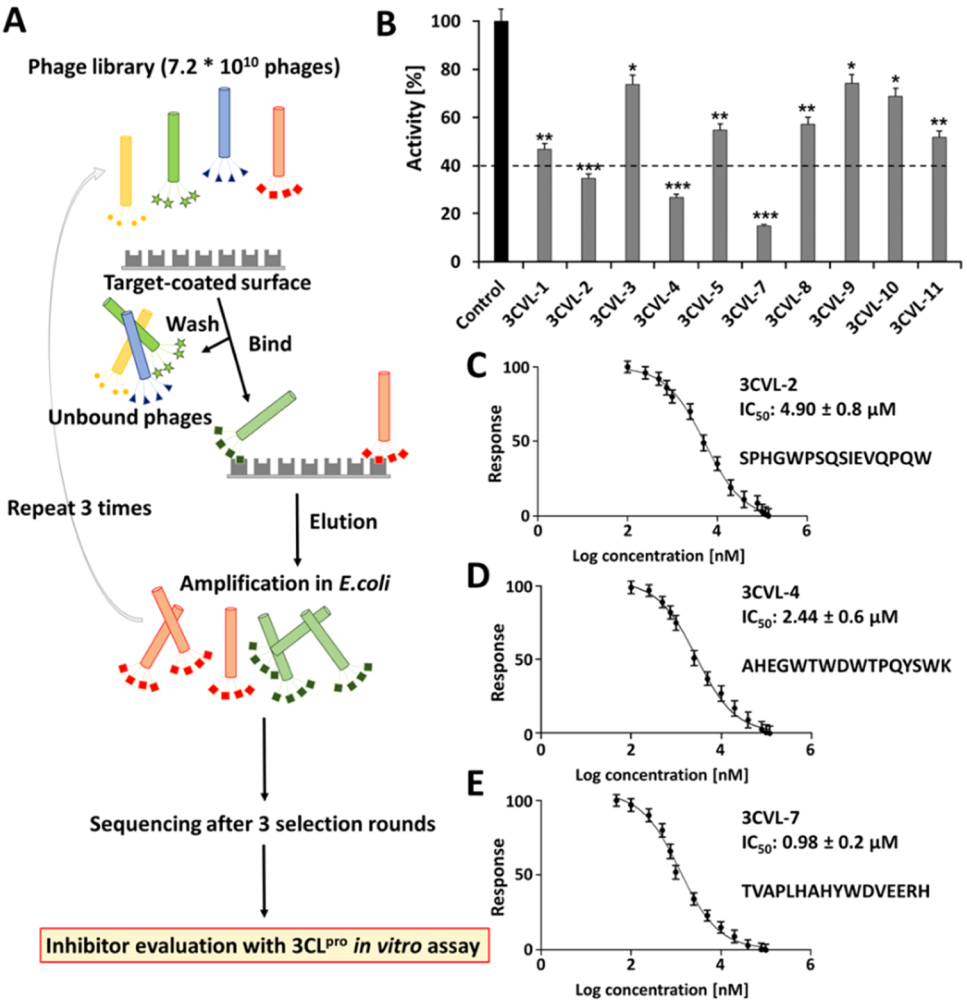

Figure 2. Phage display scheme and screening of phage display L-peptides against SARS-CoV-2 3CL^{pro} activity. (A) Schematic diagram of the phage display process. (B) Primary screen of the 11 selected peptides (10 μM) against SARS-CoV-2 3CL^{pro} activity. 3CVL-2, 3CVL-4, and 3CVL-7 inhibit the virus protease activity by more than 60%. (C–E) Selected peptide inhibiting SARS-CoV-2 3L^{pro}. Dose–response curves for IC_{50} values of 3CVL-2 (C), 3CVL-4 (D), and 3CVL-7 (E) were determined by nonlinear regression. Data shown are the mean ± standard deviation (SD) from three independent measurements ($n = 3$). Asterisks mean that the data differ from the control (0 μM inhibitor) significantly at $p < 0.05$ (*), $p < 0.01$ (**), and $p < 0.001$ (***) levels according to analyses of variance (ANOVA) and Tukey's test.

Table 1. Summary of the SARS-CoV-2 3CL^{pro} Inhibition Experiments by 3CVL-2, -4, and -7

peptide	IC_{50} (μM)	inhibition mode
3CVL-2	4.90 ± 0.8	competitive
3CVL-4	2.44 ± 0.6	noncompetitive
3CVL-7	0.98 ± 0.2	competitive

noncompetitive inhibition mode (Supporting Information, Figure S4D).

To improve the poor proteolytic stability of L-enantiomeric peptides without losing affinity and binding specificity to their target protein, the peptides 3CVL-2, 3CVL-4, and 3CVL-7 were synthesized in retro-inverse D-enantiomeric (D-ri) form and designated as 3CVLri-2, 3CVLri-4, and 3CVLri-7, respectively. Glycine does not have a chiral center that was the reason that the D-ri peptides have identical amino acid sequences, except for glycine, which was replaced by alanine. Additionally, an arginine was added to the C-termini of each D-ri peptide to increase the permeability of the peptides. The representative scheme is shown in Figure 3A,B.

Like the L-peptides, the D-ri-peptides were tested using a concentration range of up to 140 μM (3CVLri-2 and 3CVLri-4) and up to 100 μM (3CVLri-7), which showed 100% inhibition of the protease by the corresponding used final concentration (Supporting Information, Figure S5A,C,E). Based on the enzymatic assay, the IC_{50} values were determined for each D-ri peptide, displaying for 3CVLri-2 (9.09 ± 0.5 μM), 3CVLri-4 (5.36 ± 1.7 μM) and 3CVLri-7 (1.57 ± 0.2 μM) an increase of the IC_{50} values of about 2-fold compared to the L-peptides (Figure 3C–E and Table 2). The mode of inhibition of the D-ri peptides was maintained, displaying a competitive mode of 3CLVri-2 and -7 and an allosteric mode of inhibition for 3CVLri-7 (Supporting Information, Figure S5B,D,F). A sequence analysis between the preferred 3CL^{pro} cleavage sequence pattern at the substrate-binding site and the identified inhibitors demonstrated that the competitive inhibitors have a higher similarity (ranging from 62.5 to 12.5%) compared to the noncompetitive inhibitors (no similarity) (Supporting Information, Figure S6).

2.2. Competitive and Noncompetitive D-Retro-Inverso Peptides Act Cooperatively to Inhibit SARS-CoV-2 3CL^{pro}. To presume the effect of the competitive (3CVLri-2

https://doi.org/10.1021/acschembio.2c00735
ACS Chem. Biol. 2023, 18, 315–330

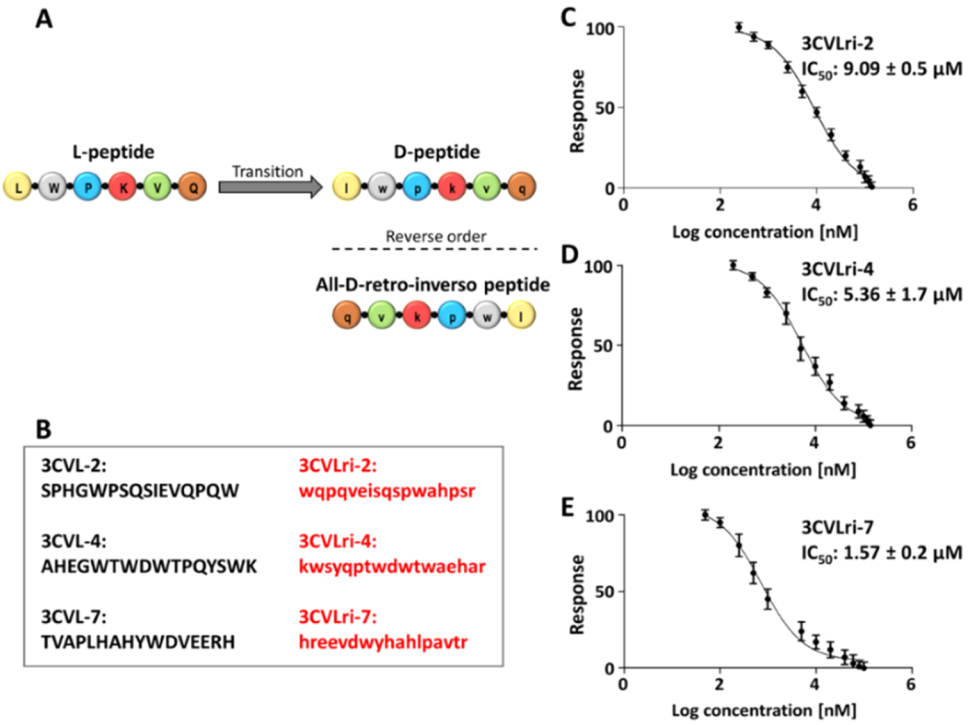

Figure 3. Principle for obtaining D-retro-inverso peptides and inhibitory effect against SARS-CoV-2 $3CL^{pro}$ activity. (A) Schematic diagram of D-retro-inverso (D-ri) peptides. (B) Sequences of 3CVLri-2, -4, -7 and their mother L-peptides. In the D-ri peptides, glycine (G) was replaced by alanine (a). (C–E) All-D-ri peptides inhibit SARS-CoV-2 $3CL^{pro}$ activity. Dose–response curves for IC_{50} values of 3CVLri-2 (C), 3CVLri-4 (D), and 3CVLri-7 (E) were determined by nonlinear regression. Data shown are the mean ± SD from three independent measurements (n = 3).

Table 2. Summary of the SARS-CoV-2 $3CL^{pro}$ Inhibition Experiments by 3CVLri-2, -4 and -7

peptide	IC_{50} (μM)	inhibition mode
3CVLri-2	9.09 ± 0.5	competitive
3CVLri-4	5.36 ± 1.7	noncompetitive
3CVLri-7	1.57 ± 0.2	competitive

and 3CVLri-7) and noncompetitive (3CVLri-4) D-retro-inverso peptides, a combined inhibitory assay was performed (3VLri-2 + 3CVLri-4 and 3CVL-7 + 3CVL-4). Both peptides were mixed in a 1:1 volume ratio and tested against the protease activity (Figure 4).

The calculated IC_{50} values for the 3CVLri-2 + 3CVLri-4 combination and the 3CVLri-7 + 3CVLri-4 combination were 0.87 ± 0.3 and 0.39 ± 0.1 μM (Figure 4A,B).

2.3. Cooperative Inhibition of SARS-CoV-2 $3CL^{pro}$ by Rupintrivir and 3CVLri-4. Rupintrivir is a known inhibitor of the 3C cysteine protease family but showed a weak inhibitory potential against the SARS-CoV-2 $3CL^{pro}$.[37−39] The determined IC_{50} value for Rupintrivir was 109 ± 14.40 μM (Figure 5A) and is in agreement with published data.[34,35] The IC_{50} value for the Rupintrivir/3CVLri-4 combination was 15.10 ± 1.60 μM (Figure 5B).

2.4. Binding Affinities of Selected $3CL^{pro}$ L- and D-Peptide Inhibitors. The interaction kinetics of 3CVL-2, -4, and -7 with $3CL^{pro}$ and its D-ri form was determined using surface plasmon resonance (SPR) experiments. $3CL^{pro}$ was immobilized via covalent primary amino group coupling, and 3CVL and 3CVLri peptides were injected as analytes. Supporting Information Figures S9 and S10 show the SPR sensorgrams for 3CVL peptides at assay concentrations of 50,

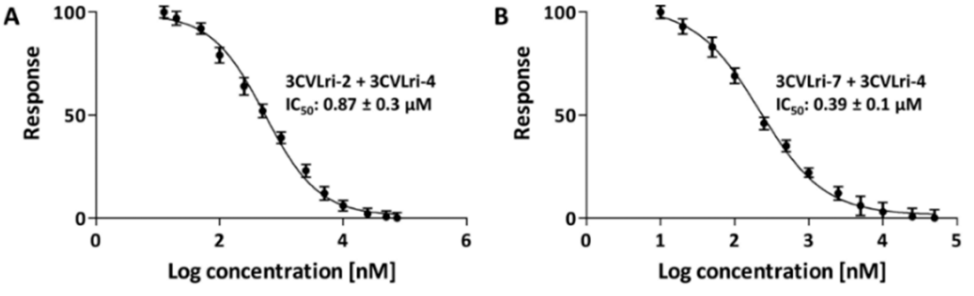

Figure 4. SARS-CoV-2 $3CL^{pro}$ inhibition by a combination of competitive and noncompetitive D-retro-inverso peptides simultaneously. Dose–response curves for IC_{50} values of the combination were determined by nonlinear regression. Data shown are the mean ± SD from three independent measurements (n = 3). The corresponding normalized activity and inhibition plots of SARS-CoV-2 $3CL^{pro}$ under the influence of the combined peptides are shown in the Supporting Information, Figure S7. (A) Dose–response curve of the 3CVLri-2 + 3CVLri-4 combination. (B) Dose–response curve of the 3CVLri-7 + 3CVLri-4 combination.

https://doi.org/10.1021/acschembio.2c00735
ACS Chem. Biol. 2023, 18, 315−330

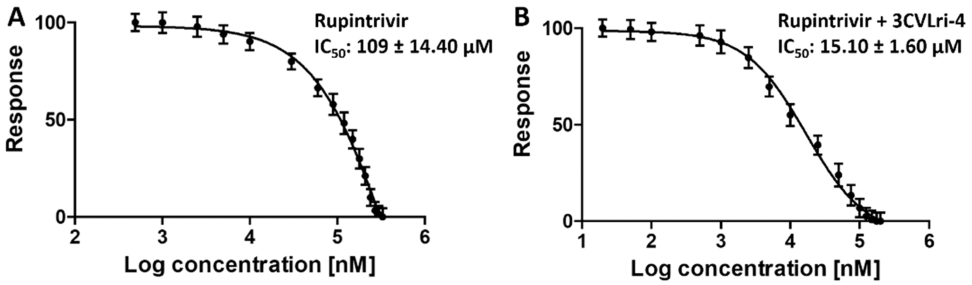

Figure 5. SARS-CoV-2 $3CL^{pro}$ inhibition by Rupintrivir and Rupintrivir/3CVLri-4 combination. Dose−response curves of the IC_{50} values were determined by nonlinear regression. Data shown are the mean ± SD from three independent measurements ($n = 3$). The corresponding normalized activity and inhibition plots of SARS-CoV-2 $3CL^{pro}$ under the influence of the combined peptides are shown in Supporting Information, Figure S8. (A) Dose−response curve of Rutinprivir. (B) Dose−response curve of the Rutinprivir/3CVLri-4 combination.

25, 12.5, 6.25, 3.12, 1.56, 0.78, and 0.39 μM on $3CL^{pro}$ immobilized on the CM5 sensor chip. The fit for the competitive inhibitors was made using a heterogeneous ligand model in which the two binding sites on the dimer are assumed to behave differently, as described for the $3CL^{pro}$ dimer active sites.[40−42] The fit for the noncompetitive inhibitor was made using a 1:1 stoichiometric kinetic fitting.

Heterogeneous ligand fitting revealed dissociation constants from the low μM to low nM range for the higher affine binding site. Global 1:1 fitting showed dissociation constants in the low μM range (Supporting Information, Figures S9 and S10 and Table 3).

Table 3. K_D Values Determined by SPR Experiments

heterogeneous ligand fitting		
peptide	K_D1	K_D2
3CVL-2	0.5 nM	6.5 μM
3CVL-7	1.8 μM	7.8 μM
3CVLri-2	46.8 μM	1.7 μM
3CVLri-7	2.4 nM	35 μM
1:1 ligand fitting		
peptide	K_D	
3CVL-4	5.1 μM	
3CVLri-4	25.2 μM	

The binding kinetic parameters of the association rate k_a, dissociation rate k_d, and dissociation constant K_D (k_d/k_a) for the interaction of $3CL^{pro}$ with peptides 3CVL-2, -4, -7, and 3CVLri-2, -4, and -7 are shown in Supporting Information, Figures S9 and S10.

2.5. 24 h Stability and Promiscuous Assays of 3CVLri Peptides. Peptide-based inhibitors targeting active proteolytic proteases can lose their inhibitory effect over time. Based on our focus, the retro-inverso peptides were tested regarding their stability over 24 h. The results demonstrated a constant inhibition of SARS-CoV-2 $3CL^{pro}$ over time, showing that the peptides are not prone to the 3CL protease digestion (Supporting Information, Figure S11). Furthermore, a detergent-based control was carried out to exclude peptide inhibitors that possibly act as an aggregator of $3CL^{pro}$, so-called "promiscuous" inhibitors. The experiment was performed by adding 0.001, 0.01, and 0.1% of Triton X-100 detergent to the reaction. Suppose that a molecule exhibits significant inhibition of $3CL^{pro}$, but this is diminished by detergent; it may act as an aggregation-based inhibitor. This was not observed for the tested 3CVLri peptides (Supporting Information, Figure S12).

2.6. Metabolic Stability of 3CVLri Peptides. To investigate the 3CVLri-2, 3CVLri-4, and 3CVLri-7 peptides' resistance against enzymatic degradation, the peptides were incubated in media simulating the gastrointestinal tract, blood, and liver, and the unmetabolized peptides were quantified by reversed-phase high-performance liquid chromatography (RP-HPLC). In simulated gastric fluid (SGF), the resistance of 3CVLri-2, 3CVLri-4, and 3CVLri-7 was monitored over 8 h. The results showed that the 3CVLri-4 and -7 peptides are relatively stable (≥80 ± 3%) within 8 h. In contrast, 3CVLri-2 was remarkably metabolized (∼75 ± 2%) (Figure 6A). The resistance of the D-ri peptides was also investigated using a simulated intestinal fluid (SIF). The peptides 3CVLri-2 and 3CVLri-4 remained rather stable over the selected time (≥90 ± 1.5%), as well as 3CVLri-7 (≥85 ± 5%) (Figure 6B). In human plasma, the stability of 3CVLri-2 and 3CVLri-7 was monitored for 48 h, with approximately 5% being metabolized (≥95 ± 4.5%). In contrast, the 3CVLri-4 showed about 21 ± 5.6% of degradation within 48 h (Figure 6C). Furthermore, human liver microsomes were monitored for 24 h, and 3CVLri-2 and 3CVLri-7 were about 5 ± 1.1% metabolized. However, 3CVLri-7 was almost 50% metabolized (≥45 ± 3.7%) in the same period (Figure 6D). The corresponding HPLC profiles of the stability tests are shown in Supporting Information, Figures S13−S16.

2.7. *In Silico* Structural Properties of 3CVL and 3CVLri Peptides and Their Similar Interaction Mode with SARS-CoV-2 $3CL^{pro}$. Protease-peptide docking and subsequent molecular dynamics (MD) simulations were performed to investigate the possible binding interface between $3CL^{pro}$-L and D-ri-peptide complexes. The secondary structure of the three-dimensional (3D) models of the L-peptides (3CVL-2, -4, and -7) and their D-ri counterparts corroborates with circular dichroism (CD) spectroscopy results.

The models are supported by the results of the inhibition assay. The inhibition mode assay identified two peptides as competitive inhibitors, which requires interaction in the active site and/or in the substrate-binding site. Another peptide was identified as a noncompetitive inhibitor, which requires interaction with an allosteric site. Indeed, the two competitive inhibitors docked in the active site formed a very stable interaction during the MD simulations. The noncompetitive inhibitor was docked in an allosteric site, which was described previously and showed a stable interaction through MD simulation.

During the 1 μs MD simulations of the unbound peptides, they mainly contained a random coiled secondary structure. However, the L- and D-ri-3CVL-4 peptides also frequently formed an α-helix (Supporting Information, Figure S17A−C).

https://doi.org/10.1021/acschembio.2c00735
ACS Chem. Biol. 2023, 18, 315−330

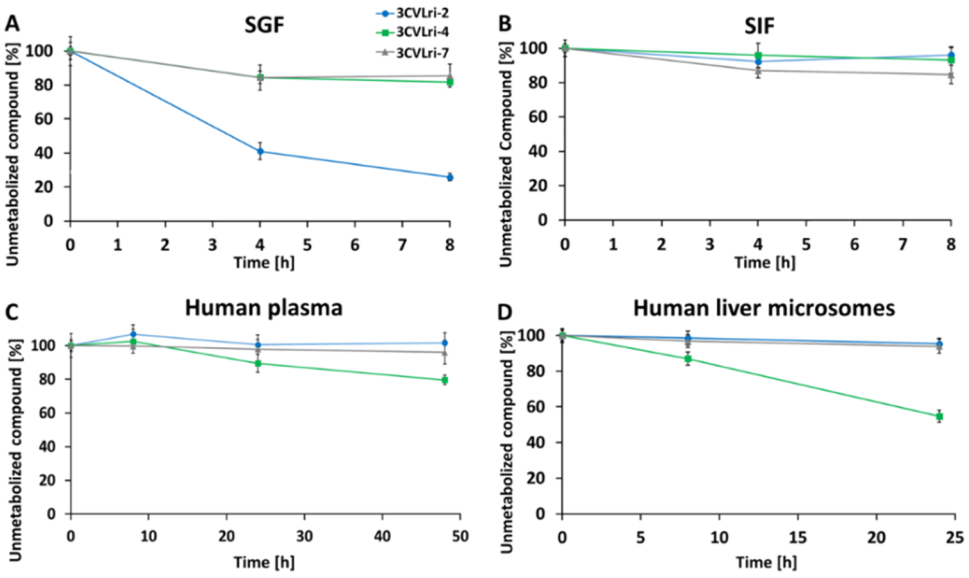

Figure 6. Stability of 3CVLri-2, 3CVLri-4, and 3CVLri-7 peptides incubated in SGF, SIF, human plasma, and human liver microsomes. (A) SGF, (B) SIF, (C) human plasma, and (D) human liver microsomes. Unmetabolized peptides were quantified by P-HPLC. The peak areas of the unmetabolized peptides after different incubation times were normalized to the peptides' peak areas after direct extraction from the media. Data are presented as mean ± SD (n = 3).

The atomic coordinates of SARS-CoV-2 3CL^{pro} dimer (PDB entry: 6M2N) and ten representative structures per peptide from the peptide simulations were submitted for docking using AutoDock Vina.[43]

The competitive peptides 3CVL-2/3CVLri-2 and 3CVL-7/3CVLri-7 were docked into the active site and substrate-binding site of the protease (Supporting Information, Table S4). The noncompetitive peptides 3CVL-4 and 3CVLri-4 were docked in a potential allosteric binding site (Supporting Information, Table S4). Previous studies have indicated that only one active site of the dimer is functional.[40,42] Based on that information, 200 ns control MD simulation of the dimer without ligands was performed to identify a potentially less stable protomer or collapsing binding sites. Based on the volume of the active sites, we did not identify any differences between both protomers (Supporting Information, Figure S18). Therefore, we docked the competitive peptides into the active site of chain A. After docking, 100 ns MD simulations with 3 different initial structures of the 3CL^{pro}/peptide complexes obtained from docking were conducted to further assess their stabilities. The initial structures were selected based on the calculated binding free energy and the distance to the critical catalytic dyad residues (Cys145 and His41). The flexibility of the peptides in complex with the protease was monitored by calculating the root-mean-square deviation (RMSD), root-mean-square fluctuations (RMSF), and ΔH as the enthalpy of binding (Supporting Information, Figures S19−S21). In all three simulations of each 3CL^{pro}/peptide complex, the peptide maintained its overall conformation in the binding pocket and no unbinding event was detected. Representative structures for all three simulations of each L- and D-ri-peptide are shown in Supporting Information, Figures S22 and S23. To investigate the 3CL^{pro} peptide interactions in more detail, we selected one of the three MD simulations per peptide based on several criteria, such as the RMSD, RMSF, and the binding free energy, elongated the simulations to 200 ns and conducted them in triplicate. Each replica of the elongated simulations showed a stable interaction between the L- and D-ri-3CVL peptides and their respective binding site of the 3CL^{pro} dimer throughout the simulation.

To identify the most popular binding modes sampled during the elongated simulations, we applied conformational clustering but considered only the nonflexible/interacting residues (RMSF ≤ 5 Å) of the peptides (Supporting Information, Figure S24).

Interactions between the residues of the peptides and the protease were analyzed by calculating the minimum distance between them for the first three clusters per complex (Table 4).

Table 4. Summary of MD Simulation Triplicates Considering Nonflexible/Interacting Residues of Peptides

peptide	#cluster	representative frames first 3 clusters (%)
3CVL-2	8	97
3CVL-4	12	88
3CVL-7	25	80
3CVLri-2	12	83
3CVLri-4	10	99
3CVLri-7	14	93

Analysis of the 3CL^{pro}-peptide complexes provides valuable information on the interaction interface similarities between 3CVL and 3CVLri peptides. Structural representation (Figure 7) demonstrated that 3CVL-2 extends along with S1′, S1, and S3 subpockets of the protease substrate-binding site (Figure 7A).

In contrast, the 3CVLri-2 interacts with the substrate-binding site differently. However, it extends along with S1′, S1, S2, and S3 (Figure 7B), which shows that one of the D-Gln residues of the 3CVLri-2 is very well accommodated. The 3CVL-7 and 3CVLri-7 interaction areas comprise residues of the S1′, S1, S2 and S3 subsites (Figure 7C,D). The graphs in Figure 7 that show the minimum distance between peptide and 3CL^{pro} residues reveal that all analyzed peptides formed several interactions with 3CL^{pro} active/binding site residues. The localization in the substrate-binding region of the 3CVL peptides and their D-ri counterparts, even when it does not interact with the catalytic

https://doi.org/10.1021/acschembio.2c00735
ACS Chem. Biol. 2023, 18, 315−330

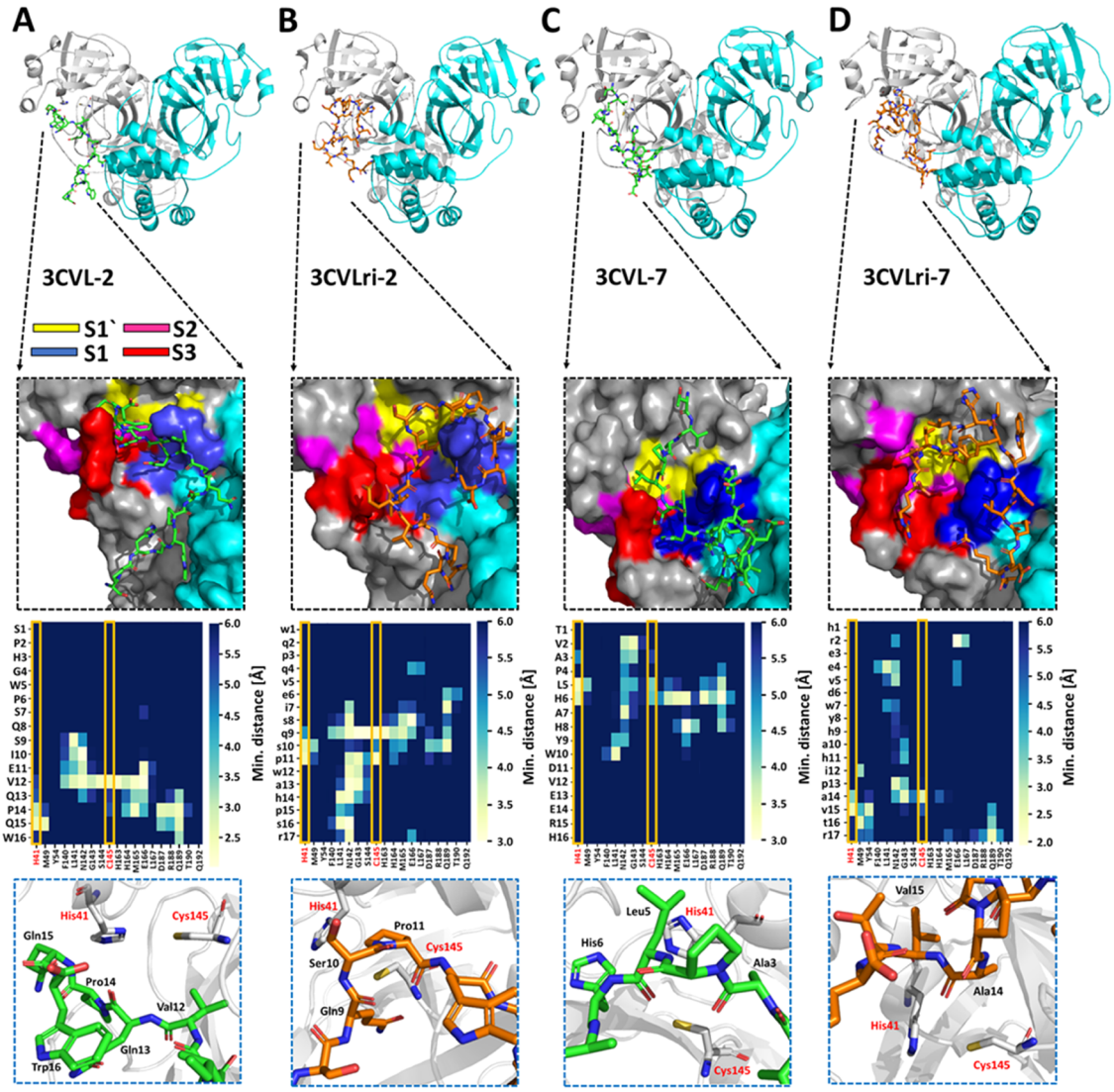

Figure 7. Comparison of the competitive 3CVL and 3CVLri peptide inhibitors binding position in the $3CL^{pro}$ active and substrate-binding site. $3CL^{pro}$ is shown in ribbon view: chain A (gray) and chain B (turquoise). The 3CVL (green) and 3CVLri (orange) peptides are shown as sticks. The surface view demonstrates a preferred position of the peptide in the substrate-binding region, and the single subsites are marked by different colors (S1′: yellow; S1: blue; S2: pink; S3: red). The distance between the $3CL^{pro}$ substrate-binding site residues and the peptides shows that active site residues His41 and Cys145 are blocked by the inhibitors: (A) 3CVL-2, (B) 3CVLri-2, (C) 3CVL-7, (D) 3CVLri-7.

dyad (His41 and Cys145), showed the potential to block the entrance of the substrate.

To investigate the impact of the competitive inhibitors 3CVL-2, 3CVLri-2, 3CVL-7, and 3CVLri-7, two-dimensional NMR 1H-15N correlation spectra of 100 μM 15N $3CL^{pro}$ were recorded in the presence of an equimolar amount of the respective peptides (1:1 ratio). Supporting Information, Figure S25A shows the reference spectrum of 15N $3CL^{pro}$ in the absence of the peptides. Spectral resonances are well resolved and display the properties of a globular protein containing both β-sheets and α-helices. Several other 15N $3CL^{pro}$ resonances appear in the presence of 3CVL-2 (orange spectrum) compared to the reference spectrum (black) (Supporting Information, Figure S25B). That could point either to a second $3CL^{pro}$ conformation becoming visible or previously invisible parts of $3CL^{pro}$ becoming more dynamic and visible in the presence of the peptide. The effect seems less intense for 3CVLri-2 (Supporting Information, Figure S25C, light blue spectrum).

The NMR spectra of 15N $3CL^{pro}$ in the presence of 3CVL-7 (Supporting Information, Figure S26B) look very similar to those for 3CVL-2; several new resonances of 15N $3CL^{pro}$ appear in the presence of 3CVL-7 and 3CVLri-7 (Supporting Information, Figure S26B,C), indicating higher conformational or overall dynamics.

Contrary, the noncompetitive inhibitors 3CVL-4 and 3CVLri-4 were docked in a suggested allosteric site at the interface of the protomers. Structural representation of the interfaces of $3CL^{pro}$ in complex with the 3CVL-4 and 3CVLri-4 peptides are shown in Figure 8A,B.

Analysis of the distance between residues of the allosteric site of each protomer demonstrated that several residues of both protomer chains interact with the protease, in particular Lys12, 97, and 100 (Figure 8).

MD simulations of 3CVL-4 and 3CVLri-4 in a proposed allosteric site showed that this interaction induces conformational changes in the protease's active site.

https://doi.org/10.1021/acschembio.2c00735
ACS Chem. Biol. 2023, 18, 315−330

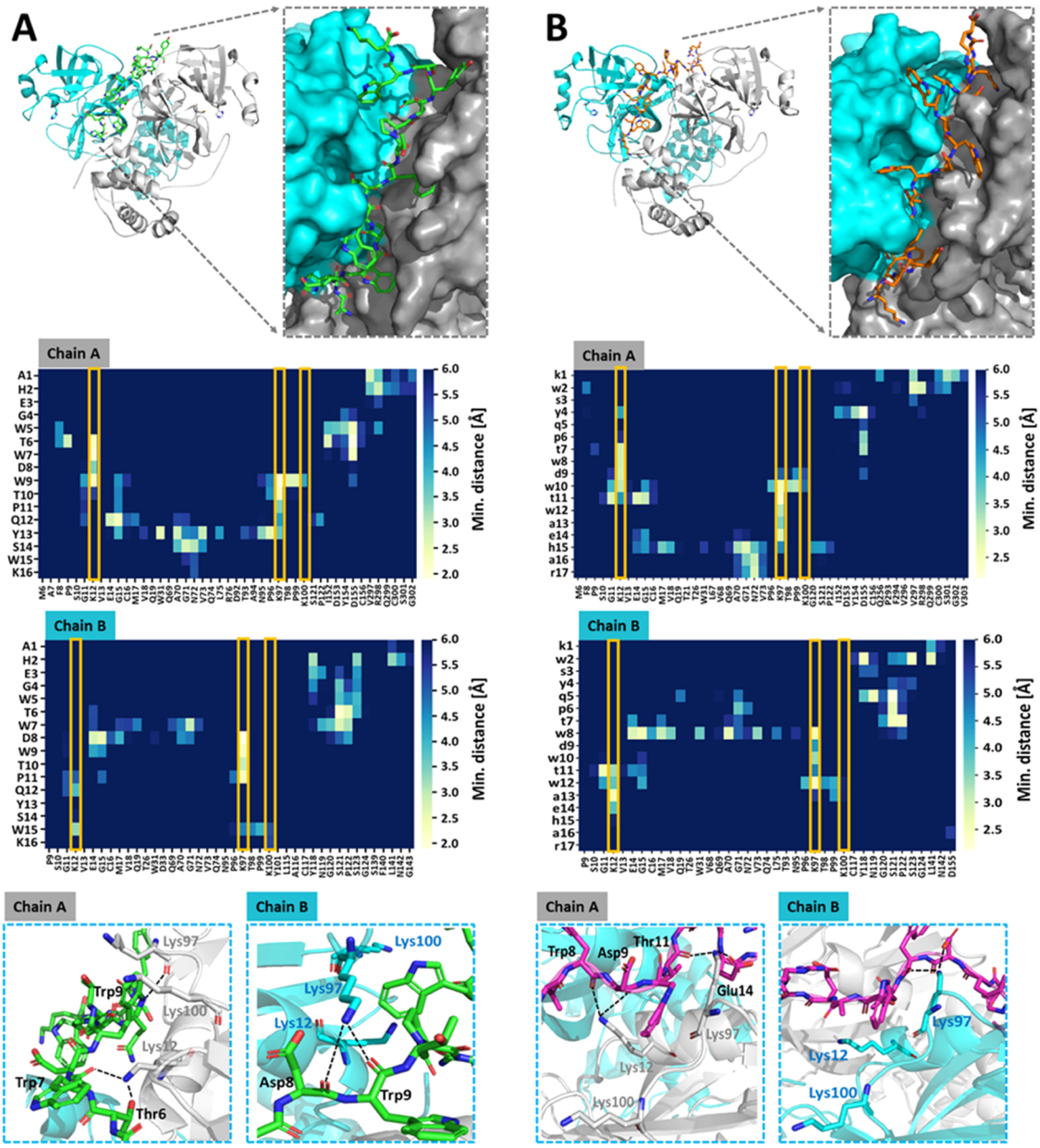

Figure 8. Comparison of the noncompetitive 3CVL-4 and 3CVLri-4 peptide inhibitors in a supposed 3CL^{pro} allosteric site. 3CL^{pro} is shown in ribbon view, and each protomer is colored differently: chain A (gray) and chain B (turquoise). 3CVL (green) and 3CVLri (orange) peptides are shown as sticks. The surface view demonstrates a preferred position of the peptide in the proposed allosteric site in a cleft between both protease protomers: (A) 3CVL-4 and (B) 3CVLri-4.

Determination of B-chain active site volume demonstrates a reduction compared to the control simulation due to the binding of 3CVL-4 and 3CVLri-4, respectively (Figure 9A–C and Supporting Information, Figure S27).

To determine the contribution of specific residues of the 3CVL and 3CVLri peptides to the interaction with 3CL^{pro} we performed a mutational analysis using alanine scanning. Alanine mutations that result in positive $\Delta\Delta H$ values relative to the parent structure suggest loss of binding, which indicates that the mutated amino acid was involved in an overall favorable network of electrostatic interactions. Mutations that result in negative $\Delta\Delta H$ suggest gain of binding, which indicates that the mutated amino acid was involved in an overall unfavorable network of electrostatic interactions.

In the case of 3CVLri-2 and its parental L-peptide Gln9 and Gln8, respectively, are important for the interaction with 3CL^{pro}. The Ser8 residue (Ser7 in the L-peptide) situated at the P2 position seems to have a weak effect on the interaction with 3CL^{pro} (Supporting Information, Figure S28A). The glutamine residues are in the P1 position of the peptides, as in the substrate already described for the protease, the P2 site has a preference for hydrophobic residues (Supporting Information, Figure S6). Important residues in the interaction between 3CVLri-7 (3CVL-7) and 3CL^{pro} are His9 (His6) and His11 (His8), unfavorable residues are Asp6 (Asp11) and Ala10 (Ala7) (Supporting Information, Figure S28A). In the case of the noncompetitive inhibitors, 3CVLri-4 (3CVL-4), Trp8 (Trp9), and Tyr4 (Tyr13) are mainly involved in the interaction with the virus protease. Interestingly, Asp8 in the mother L-peptide

https://doi.org/10.1021/acschembio.2c00735
ACS Chem. Biol. 2023, 18, 315−330

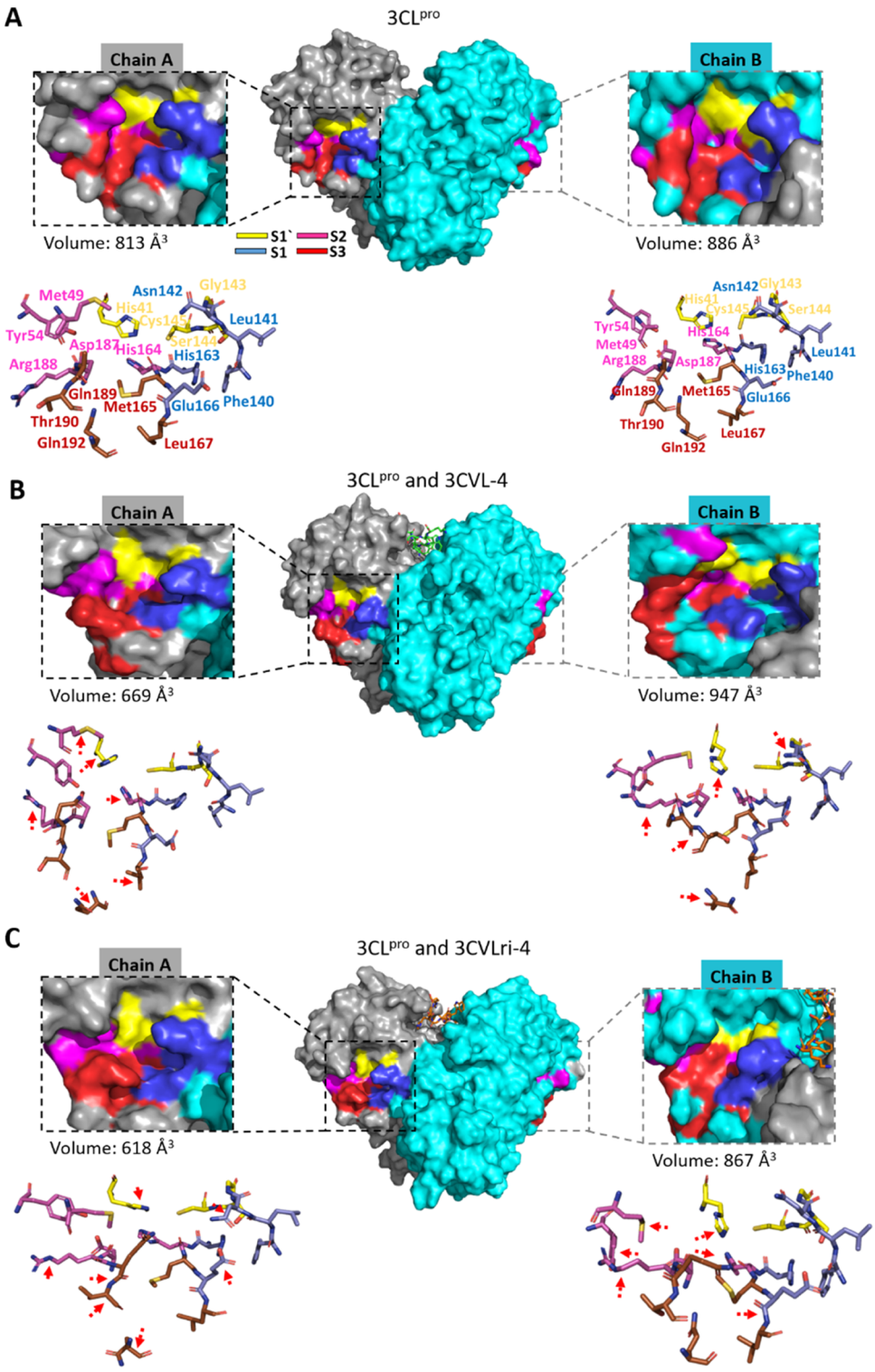

Figure 9. Comparison of the active site volumes of control and after binding of the noncompetitive 3CVL-4 and 3CVLri-4 peptide inhibitors in a supposed $3CL^{pro}$ allosteric site. $3CL^{pro}$ is shown in surface view, and each protomer is colored differently: chain A (gray) and chain B (turquoise). The substrate-binding subsites are colored differently. The active sites and substrate-binding sites of each protomer are shown enlarged with the corresponding volume in $Å^3$. Amino acids forming the active site and substrate-binding site are shown in sticks, red arrows demonstrate the change of the position of the residues because of the conformational change induced by the noncompetitive inhibitors: (A) $3CL^{pro}$, (B) $3CL^{pro}$ and 3CVL-4, (C) $3CL^{pro}$ and 3CVLri-4.

(Supporting Information, Figure S28B) is unfavorable for the interaction, but the corresponding residue in the D-ri peptide is involved in the interaction with $3CL^{pro}$.

3. DISCUSSION AND CONCLUSIONS

Even with the development of several vaccines against SARS-CoV-2, the development of suitable therapeutics against COVID-19 is important since no causative therapy is known.

https://doi.org/10.1021/acschembio.2c00735
ACS Chem. Biol. 2023, 18, 315−330

Instead of inhibiting the interaction of the spike protein with the cell receptors,[44,45] we intend to target one of the most important proteases in virus replication, the 3CL protease, by D-enantiomeric peptide ligands preventing the cleavage function of 3CL^{pro}. To this end, a phage display selection was performed. The identified L-peptides showed a strong inhibitory effect in the enzyme activity assay, with IC_{50} values varying between 0.9 and 9 μM. As we demonstrated experimentally, 3CVL-4 is a noncompetitive inhibitor with an IC_{50} value of 2.4 μM, which was maintained in its D-enantiomer retro-inverso form; however, with an increased IC_{50} value of about 2-fold (5.4 μM). A 1:1 molar combination of the competitive and noncompetitive D-ri-peptides reduced the IC_{50} values remarkably. 3CVLri-2 + 3CVLri-4 combination reduces the IC_{50} value to 0.9 μM and the combination of 3CVLri-7 + 3CVLri-4 to 0.4 μM. It was clearly demonstrated that a combination of competitive and non-competitive inhibitors improved the inhibitory potential of all D-peptides. Similarly, in combination with Rupintrivir, a weak SARS-CoV-2 3CL^{pro} competitive inhibitor (IC_{50} > 100 μM), the inhibitory effect improved after the combination with the noncompetitive 3CVLri-4 (IC_{50} of 15.10 ± 1.60 μM). The cooperative inhibition of SARS-CoV-2 3CL^{pro} by competitive and noncompetitive inhibitors was also observed for Quinacrine/Suramin.[42] The structural analysis of 3CL^{pro} in complex with the studied peptides by docking followed by molecular dynamics simulation predicted a stable conformation for each complex, indicating significant intermolecular interaction. Of note, when not directly interacting with the catalytic dyad, amino acid residues of the peptide are located close to the pocket entry, blocking the substrate entrance. The predicted structures of 3CL^{pro} in complex with 3CVLri-2 indicate the occurrence of significant intermolecular interaction between the D-glutamine of the all-D-ri peptide and amino acid residues of the S1 subpocket, which explains the strong preference for D-glutamine at P1.[46]

A combination of competitive and noncompetitive D-ri-peptides (3CVLri-2/3CVLri-4 and 3CVLri-7/3CVLri-4) increased the inhibitory effect against 3CL^{pro}.

The all-D-peptides 3CVLri-2 and -7 showed a remarkable resistance against metabolization over 8 h.

Two-dimensional 1H-15N TROSY-NMR correlation spectra of 15N 3CL^{pro} with 3CVL-2/3CVLri-2 and 3CVL-7/3CVLri-7 demonstrated the appearance of new and similar resonances, which may indicate the same binding region for the peptides.

Our study yielded all-D-peptides with a promising potential for further development toward therapeutic use against SARS-CoV-2 3CL^{pro}.

4. MATERIALS AND METHODS

4.1. Peptides. All peptides were purchased from Caslo (Lyngby, Denmark) as a lyophilized powder with >98% purity. Peptides 3CVL 1−10 consist of 16 amino acid residues in L-configuration with amidated C-termini. The D-retro-inverso (D-ri) peptides 3CVLri-2, 3CVLri-4, and 3CVLri-7 have identical amino acid sequences, except for glycine, which was replaced by alanine in the case of 3CVLri-2 and 3CVLri-4. All amino acid residues in D-configuration and with a reversal peptide bond. Additionally, an arginine was added to the C-termini of each ri-peptide resulting in 17 amino acid residues. The C-termini of the D-ri-peptides are amidated, and the N-termini are acetylated. An analysis certificate from Caslo (Lyngby, Denmark) demonstrated the purity of each peptide (Supporting Information, Figures S29−S32 and Table S5). High-performance liquid chromatography (HPLC) analysis was performed with a C18 column. For the mass spectrometry certificate, the matrix-assisted laser desorption ionization time-of-flight (MALDI-TOF) method was used.

4.2. Protein Expression and Purification. SARS-CoV-2 3CL^{pro} (Uniprot entry: P0DTD1, virus strain: hCoV-19/Wuhan/WIV04/2019) was cloned, expressed, and purified as described previously.[41]

4.3. Phage Display. Two independent phage display selections (selection A and B), each with three rounds, were performed to obtain peptides that bind 3CL^{pro}. Therefore, in both selections, 100 μg/mL purified 3CL^{pro} diluted in 100 μL of 20 mM potassium phosphate buffer pH 7.5 with 150 mM sodium chloride were immobilized on an amino plate (Nunc Amino Immobilizer 96-well plates, polystyrene; Thermo Scientific, Waltham). After 30 min at room temperature (RT), the 3CL^{pro} solution was removed, and the surface was quenched with 1 M ethanolamine pH 8.5 (Cytiva; Chicago) for 1 h at RT. Additionally, the surface was blocked with 200 μL of 10 mg/mL BSA in 20 mM potassium phosphate buffer pH 7.5 with 150 mM sodium chloride in the first round and with 200 μL of 10 mg/mL milk powder in 20 mM potassium phosphate buffer pH 7.5 with 150 mM sodium chloride in the second round to reduce unspecific binding events. In the third round, the surface was not additionally blocked to vary the selection conditions. The surface was washed six times with 200 μL of washing buffer (20 mM potassium phosphate buffer pH 7.5 with 150 mM sodium chloride and 0.05% tween-20). During the first and second rounds, 2 mg/mL BSA or milk powder was added to the washing buffer, respectively. Then, 7.2×10^{10} phages (TriCo-16 phage display peptide library; Creative Biolabs, New York) in 100 μL of the corresponding washing buffer were added and incubated for 20 min at RT with the exception of the third round of selection B. Here, the incubation time was extended to 30 min. After removing of nonbinding phages, the well was washed with 200 μL of the respective washing buffer of the corresponding round. The number of washing steps was varied in each selection round (selection A: 2-5-5; selection B: 5-8-10). Elution of phages was performed by incubation with 100 μL of 0.2 M Glycine-HCl pH 2.2 for 10 min at RT. The phage-containing solution was then removed from the plate and neutralized by transferring it to a tube containing 25 μL of 1 M Tris-HCl pH 9.1. To determine the output titer, 5 μL of eluted phages were used. Therefore, a dilution series from 10-2 to 10-8 was prepared with the eluted phages in a total volume of 100 μL of LB medium. Each dilution was mixed with 100 μL of *Escherichia coli* K12 ER2738 (OD600 of 0.6) and plated with 800 μL of top agar on plates (35 × 10 mm; Sarstedt, Nümbrecht, Germany) containing LB-Agar-IPTG-XGal. After overnight incubation at 37 °C, the plaques were counted to determine the output titer.

The remaining eluted phages (120 μL) were amplified in 20 mL of *E. coli* K12 ER2738, starting with an OD_{600} of 0.1 for 3.5 h at 37 °C and 120 rpm. The culture was then centrifuged for 20 min at 2700*g* and 4 °C. The pellet was discarded, and the supernatant was incubated with 7 mL of PEG-8000/2.5 M sodium chloride overnight at 4 °C for phage precipitation. Subsequently, the solution was centrifuged for 1 h at 4 °C, and 2700*g*. The phage-containing pellet was dissolved in 1 mL of 1 × phosphate-buffered saline (PBS) before another centrifugation step at 4 °C and 11,000*g* for 5 min to get rid of residual bacterial components. Afterward, the supernatant was added to 200 μL of PEG-8000/2.5 M sodium chloride and incubated for 1 h on ice, followed by final centrifugation for 45 min at 2700*g* and 4 °C. The phage-containing pellet was properly resuspended in 100 μL of 1 × PBS. The input titer was determined by spectrophotometry[40] in 1 × PBS using a 1:10 dilution. The resulting phages were then used in the next selection round with the same phage amount as before and further used for an enrichment enzyme-linked immunosorbent assay (ELISA) and prepared for next-generation sequencing (NGS) analysis.

Besides the primary selection with 3CL^{pro} as the target (Target Selection, TS), two control selections were performed as described before[46] to enable an efficient evaluation of the selection success and to facilitate further the identification of target-binding peptides over those peptides that have accumulated, e.g., because of an affinity to the surface. The first control selection, called Empty Selection (ES), was performed in the same way as TS but without 3CL^{pro}. During immobilization, 20 mM potassium phosphate buffer pH 7.5 with 150 mM sodium chloride was used instead of 3CL^{pro}. One further control,

https://doi.org/10.1021/acschembio.2c00735
ACS Chem. Biol. 2023, 18, 315−330

Direct Control (DC), was performed starting from the second round without 3CL^{pro}, but in contrast to ES, the phages resulting from each round of TS were used for the following selection rounds.

4.4. Enrichment ELISA. An enrichment ELISA was performed to validate the success of the phage display selection. Therefore, 100 μg/mL 3CL^{pro} diluted in 100 μL of 20 mM potassium phosphate buffer pH 7.5 with 150 mM sodium chloride was immobilized on an amino plate (Nunc Immobilizer Amino 96-well plate, polystyrene; Thermo Scientific, Waltham) for 30 min at RT. Noncoated wells (20 mM potassium phosphate buffer pH 7.5 with 150 mM sodium chloride without 3CL^{pro}) were used as a control for each selection round. The solution was removed, and the surface was quenched with 200 μL of 1 M ethanolamine pH 8.5 (Cytiva; Chicago) for 1 h at RT, followed by a blocking step with 200 μL of blocking solution (10 mg/mL BSA in 20 mM potassium phosphate buffer pH 7.5 with 150 mM sodium chloride) for 15 min at RT. After three washing steps with 200 μL of washing buffer (150 mM sodium chloride, 0.05% Tween-20, 2 mg/mL BSA in 20 mM potassium phosphate buffer pH 7.5), the amplified and purified phages of each target selection round were diluted in washing buffer to a total amount of 5×10^{10} phages in 100 μL. The wells immobilized with 3CL^{pro} and noncoated wells were incubated with the corresponding phage solution for 1 h at RT. Unbound phages were removed by five washing steps with 150 μL of washing buffer. The anti-M13 antibody (HRP conjugated mouse monoclonal antibacteriophage M13 antibody; Sino Biological, Peking, China) was diluted in washing buffer to a final concentration of 0.35 ng/μL, and 100 μL was added to each well for 1 h at RT. After 6 washing steps with 150 μL of washing buffer, the supernatant was removed entirely, and 100 μL of the 3,3′,5,5′-tetramethylbenzidine (TMB) solution (TMB was previously dissolved in 1 mL of dimethyl sulfoxide (DMSO) and diluted with 9 mL of 0.05 M phosphate citrate buffer pH 5) were added into each well. After 2.5 min incubation at RT, the reaction was stopped with 100 μL of 2 M H_2SO_4. The absorption was quantified at 450 nm using a microplate reader (BMG Labtech, Ortenberg, Germany).

In addition to the samples from the target selection (TS1, TS2, TS3), the library and the wild-type phage without peptides were analyzed. The measurement was performed in single determination to save protein samples. Noncoated wells that were incubated with washing buffer without phages were used as a control for the background signal.

4.5. Sequence Analysis. Extraction and the amplification of the single-stranded phage DNA from each sample from the phage display selection were purified and prepared for NGS analysis as described previously.[46] NGS analysis was performed by the Biologisch-Medizinisches Forschungszentrum at the Heinrich Heine University Düsseldorf, Germany. The resulting sequences were further processed and evaluated with the targeted sequencing analysis tool (TSAT) and the open-source software Hammock for subsequent sequence alignment.[47,48]

4.6. SARS-CoV-2 3CL^{pro} Activity Assay. SARS-CoV-2 3CL^{pro} activity assay was performed as described previously.[42,49−51] A fluorogenic substrate DABCYL-KTSAVLQ↓SGFRKME-EDANS (Bachem, Bubendorf, Switzerland) was used, and the assay buffer contained 20 mM Tris pH 7.2, 200 mM NaCl, 1 mM ethylenediaminetetraacetic acid (EDTA), and 1 mM tris(2-carboxyethyl)-phosphine (TCEP). The reaction mixture was pipetted in a Corning 96-Well plate (Merck, Darmstadt, Germany) consisting of 0.5 μM 3CL^{pro}. The assay was initiated with the addition of the substrate at a final concentration of 50 μM. The fluorescence intensities were measured at 60 s intervals over 30 min using an Infinite 200 PRO plate reader (Tecan, Männedorf, Switzerland), and the temperature was set to 37 °C. The excitation and emission wavelengths were 360 and 460 nm, respectively.

4.7. SARS-CoV-2 3CL^{pro} Inhibition Assay. Inhibition of SARS-CoV-2 3CL^{pro} activity by 3CVL-1 to 10 and 3CVLri-2, -4, and -7 was investigated using the described activity assay. The L-Peptides (10 μM) were used for a preliminary screening test. For the final inhibition assays, 0.5 μM protein was incubated with 0−140 μM 3CVL-2, 0−120 μM 3CVL-4, and 0−100 μM 3CVL-7. The corresponding 3CVLri peptides were incubated with the same inhibitor concentrations, except for 3CVLri-4 (0−140 μM). The mixtures were incubated for 30 min at RT. When the substrate with a final concentration of 50 μM was added to the mixture, the fluorescence intensities were measured at 60 s intervals over 30 min using an Infinite 200 PRO plate reader (Tecan, Männedorf, Switzerland). The temperature was set to 37 °C, and the excitation and emission wavelengths were 360 and 460 nm, respectively. Inhibition assays were performed as triplicates.

For the 3CVLri-2 + 3CVLri-4 and 3CVLri-4 + 3CVLri-7 combination tests, a 1:1 stock solution of the molecules was prepared. Protein (0.5 μM) was incubated with 0−75 μM (3CVLri-2 + 3CVLri-4) and 0−50 μM (3CVLri-4 + 3CVLri-7) of the combined molecules. The IC_{50} values were calculated by plotting the initial velocity against various concentrations of the peptides using a dose−response curve in GraphPad Prism software version 8 (San Diego, CA). Data are presented as mean ± SD.

4.8. Determination of Inhibition Mode. The inhibition mode was determined using different final concentrations of the inhibitors and substrate. Briefly, 0.5 μM SARS-CoV-2 3CL^{pro} was incubated with the inhibitor, in various concentrations, for 30 min at RT. Subsequently, the reaction was initiated by adding the corresponding concentration series of the substrate. The data were analyzed using a Lineweaver−Burk plot; therefore, the reciprocal of velocity (1/V) vs the reciprocal of the substrate concentration (1/[S]) was compared.[52,53] All measurements were performed in triplicate, and data are presented as mean ± SD.

4.9. Inhibitor Stability over 24 h. Stable inhibition of SARS-CoV-2 3CL^{pro} by 3CVLri-2, -4, and -7 was followed via a 24 h inhibition experiment. Briefly, 0.5 μM SARS-CoV-2 3CL^{pro} was incubated with 5 μM (D-ri peptides 2 and 4) and 20 μM (D-ri peptide 7) and incubated for 1/2, 1, 2, 3, 4, 5, and 24 h at RT. The control was performed with 3CL^{pro} without the peptides and measured together after each time point. Subsequently, the reaction was initiated by the addition of the substrate. All measurements were performed in triplicate, and data are presented as mean ± SD.

4.10. Assay to Exclude D-ri Peptides as Promiscuous Inhibitors. A detergent-based control assay was performed to exclude inhibitors that possibly act as promiscuous aggregators of the 3CL^{pro} by adding 0.001, 0.01, and 0.1% of Triton X-100 to the reaction.[54] Four concentrations of 3CVLri-2 (1, 5, 10, and 20 μM), 3CVLri-4 (1, 5, 10, and 20 μM), and 3CVLri-7 (0.25, 0.5, 1, and 5 μM) were tested. All measurements were performed in triplicate, and data are presented as mean ± SD.

4.11. Circular Dichroism Spectroscopy. Circular dichroism (CD) measurements were carried out with a Jasco J-1100 spectropolarimeter (Jasco, Germany). Far-UV spectra were measured between 190 to 260 nm using 5 μM 3CL^{pro} in 20 mM K_2HPO_4/KH_2PO_4 pH 7.4 and a single peptide concentration of 30 μM in H_2O. The secondary structure of 3CVL-2, 3CVL-4, 3CVL-7, and the related D-ri peptides was checked. A 1 mm path length cell was used for the measurements; 15 repeat scans were obtained for each sample, and five scans were conducted to establish the respective baselines. The averaged baseline spectrum was subtracted from the averaged sample spectrum. The results are presented as molar ellipticity [θ], according to eq 1

$$[\theta]\lambda = \theta/(c^{*}0.001^{*}l^{*}n) \quad (1)$$

where θ is the ellipticity measured at the wavelength λ (deg), c is the peptide concentration (mol/L), 0.001 is the cell path length (cm), and n is the number of amino acids.

4.12. Surface Plasmon Resonance Measurements. Surface plasmon resonance (SPR) measurements with 3CVL peptides and SARS-CoV-2 3CL^{pro} were performed using a Biacore 8K device (GE Healthcare, Uppsala, Sweden). Recombinant 3CLpro was immobilized on a CM5 sensor surface (GE Healthcare, Uppsala, Sweden) via covalent coupling of primary amino groups. The protease was diluted to a final concentration of 15 μg/mL in 10 mM NaAc pH 5.5 and injected for 600 s at 10 μL/min to reach a final immobilization level of 2700 to 3000 RU. After quenching with Ehanolamine at pH 8.5, kinetic experiments were performed as parallel injections on all eight flow channels. 3CVL and 3CVLri peptides were diluted in 20 mM Tris pH 7.4, 100 mM NaCl, 1 mM EDTA and 0.05% Tween-20 in the

https://doi.org/10.1021/acschembio.2c00735
ACS Chem. Biol. 2023, 18, 315−330

concentration range of 0.03−50 μM with a 1:1 dilution series and injected at 30 μL/min. Surface regeneration was performed after dissociation ended for 2 × 45 s at 30 μL/min using an acidic regeneration solution consisting of 150 mM oxalic acid, 150 mM phosphoric acid, 150 mM formic acid, and 150 mM malonic acid at pH 5.0. Data evaluation was performed using a heterogeneous ligand fit model for the competitive inhibitors with Biacore Insight Evaluation Software v3.0.12 (GE Healthcare, Uppsala, Sweden). The heterogeneous ligand model assumes analyte binding at two independent ligand sites. Each ligand site binds the analyte independently and with a different rate constant. A global 1:1 kinetic fit model was used for the noncompetitive inhibitor.

4.13. Nuclear Magnetic Resonance. Two-dimensional 1H-15N TROSY-NMR correlation spectra[55] of 100 μM 15N $3CL^{pro}$ dissolved in 20 mM MES pH 6.5 buffer containing 150 mM NaCl were recorded in the presence and absence of 3CVL-2 and 3CVLri-2 as well as 3CVL-7 and 3CVLri-7 peptides. Experiments for 3CVL-4 and 3CVLri-4 could not be performed because of the peptide's instability at pH 6.5. Spectra were recorded on a Bruker 1.2 GHz AVANCE neo spectrometer equipped with a triple-resonance 1H,15N,13C cryogenic probe. The experimental temperature was 25 °C. Spectral dimensions were 16.02 ppm (1H) × 32.89 ppm (15N), with 1024 complex points recorded in the 1H dimension and 64 complex points recorded in the 15N dimension, and the Echo/Anti-echo scheme used for quadrature detection, resulting in an acquisition time of 53.2 ms in the 1H dimension and 16 ms in the 15N dimension. The carrier was positioned at 4.7 ppm in the 1H dimension and 117 ppm in the 15N dimension; 512 scans were recorded for each increment, with a recovery delay of 1 s between scans, resulting in an overall experimental time of 19.7 h per spectrum.

To study the interaction between $3CL^{pro}$ and the various peptides, only the protease was 15N-labeled and, therefore, NMR-visible, while the peptides were unlabeled and invisible in the 1H-15N correlation spectra. For the interaction study, 100 μM 15N-labeled $3CL^{pro}$ was mixed with an equimolar amount of the respective peptide. Spectra were overlayed and compared to the reference spectrum of $3CL^{pro}$ (equal final concentration, in the absence of the peptide). Spectra analysis was performed using the software Bruker Topspin 4.1.3. and CCPN Analysis 3.0.[56]

4.14. Metabolic Stability. Metabolic stability experiments of the 3CVLri peptides were performed as described before.[57,58] Solutions simulating gastric and intestinal fluid (SGF and SIF) were prepared according to the European Pharmacopoeia 7.0. Human plasma samples were purchased from Innovative Research (Novi, Michigan), and human liver microsomes were purchased from Sekisui XenoTech (Kansas City; H1000). The liver microsomes were diluted in an NADPH regenerating system (NRS). For the stability tests, 150 μM 3CVLri peptides were incubated in SGF, SIF, human plasma, and human liver microsomes in triplicate at 37 °C with slight shaking for different periods. The peptides were extracted by precipitating the proteins with a solution containing acetonitrile and 0.5% formic acid. Afterward, the mixture was mixed and heated for 5 min at 95 °C. The sample was subsequently centrifuged at 14.000*g* for 10 min at 4 °C. The extracted peptides are in the supernatant and were analyzed by reversed-phase high-performance liquid chromatography (RP-HPLC). The RP-HPLC system (Agilent Technologies, Santa Clara; 1260 series) consisted of an autosampler, quaternary pump, a thermostatted column compartment, and a variable-wavelength detector. Chromatography was performed with a C18 column (Agilent Technologies, Santa Clara; ZORBAX 300SB-C18 5 μm, 4.6 × 250 mm) at 25 °C and 214 nm with a flow rate of 1 mL/min. The sample injection volume was 20 μL. Chromatograms were recorded and analyzed with the Agilent software OpenLab version 2−5. Mobile phases were acetonitrile + 0.1% trifluoroacetic acid (TFA) (A) and water + 0.1% TFA (B) for sample analysis from stability tests. The samples were measured with an initial isocratic step at 15% solvent A for 3 min followed by a gradient elution to 45% A in 15 min. All measurements were performed in triplicate, and data are presented as mean ± SD.

4.15. Statistical Analysis. All data are expressed as the mean ± standard deviations (SDs). The statistical significance of the mean values' differences was assessed with one-way analyses of variance (ANOVA), followed by Tukeys' multiple comparison test. Significant differences were considered at $p < 0.05$ (*), $p < 0.01$ (**), and $p < 0.001$ (***). All statistical analyses were performed with GraphPad Prism software version 8 (San Diego, CA).

4.16. Docking and Molecular Dynamics. *4.16.1. Peptide and Protein Structure Preparation.* The peptide models were constructed as linear chains using the python module PeptideBuilder.[59] To obtain D-retro-inverso (D-ri) peptides, the peptides were first generated as L-retro-inverso molecules, followed by the inversion of their stereochemical configuration by flipping the structure files with cartesian coordinates along the *x*-axis. The sequences of the peptides are shown in Table 5.

Table 5. Sequences of 3CVL and 3CVLri Peptide Models

peptide	sequence
3CVL-2	SPHGWPSQSIEVQPQW
3CVL-4	AHEGWTWDWTPQYSWK
3CVL-7	TVAPLHAHYWDVEERH
3CVLri-2	wqpqveisqspwahpsr
3CVLri-4	kwsyqptwdwtwaehar
3CVLri-7	hreevdwyhahlpavtr

The initial structural data of the $3CL^{pro}$ dimer were obtained from a crystal structure (PDB: 6M2N).

4.16.2. Docking of the Peptides against the $3CL^{pro}$ Dimer. 3CVL-2, 3CVL-7, 3CVLri-2, and 3CVLri-7 were docked against the active site of chain A of the $3CL^{pro}$ dimer (PDB: 6M2N), which can be defined by the residues His41, Met49, Tyr54, Phe140, Leu141, Asn142, Gly143, Ser144, Cys145, His163, His164, Met165, Glu166, Leu167, Asp187, Arg188, Gln189, Thr190, and Gln192.[60]

3CVL-4 and 3CVLri-4 bind $3CL^{pro}$ allosterically, and both peptides were docked against the potential binding site residues Lys12, Lys97, Lys100, Tyr101, Lys102, Phe103, Val104, and Arg105.[36] Autodock Tools[61,62] were used to generate a docking grid around the positions of the binding site residues of the $3CL^{pro}$ dimer. The grid was centered at *x*,*y*,*z*-position of −33.572, −62.854, 40.9 (Active site) and −49.16, −47.323, 38.911 (Allosteric binding site). After adding hydrogen atoms to the $3CL^{pro}$ dimer and the peptides, Gasteiger partial charges were computed and added to the dimer and the peptides using AutoDock Tool. The protein and peptide models were saved in the PDBQT format. The docking was then performed using AutoDock Vina,[43] which treats the ligand as flexible while keeping the receptor rigid.

4.16.3. Simulation Setup and Production Run. All MD simulations and analyses were performed with GROMACS 2021.4.[63] AMBER14SB[64] was used as a force field, and the TIP3P water model[65] for explicit water simulation. The peptides and the protein−peptide complexes were centered in a dodecahedron box with 240.8−370.5 and 872.5 nm^3, solvated with water, and neutralized with Na^+ and Cl^- ions resulting in a system size of ∼23,500−36,000 and ∼86,000 atoms, respectively.

The systems' energy was minimized using the steepest descent algorithm.[66] The systems were then equilibrated in two steps. First, a 0.1 ns simulation was performed in the *NVT* ensemble, and second, a 1 ns simulation in the *NpT* ensemble at 310 K—velocity-rescaling thermostat[67] and 1.0 bar—Berendsen barostat.[68] First, 1 μs peptide MD simulations were performed. After the peptides were docked against the $3CL^{pro}$ dimer, we performed 100 ns of protein−peptide complexes with the temperature set to 310 K (Nosé−Hoover thermostat)[69] and the pressure set to 1 bar (Parinello−Rahman barostat).[70] One selected simulation of each protein−peptide complex was then extended to 200 ns and ran in triplicates.

Electrostatic interactions were processed with the particle-mesh Ewald method,[71,72] combined with periodic boundary conditions and a real-space cutoff of 12 Å. The same cutoff was applied to Lennard-Jones (LJ) interactions. The leapfrog stochastic dynamics integrator was used with a time step of 2 fs to integrate the equations of motion. During the

https://doi.org/10.1021/acschembio.2c00735
ACS Chem. Biol. 2023, 18, 315−330

MD simulations, all bond lengths were constrained using the LINCS algorithm.[73]

4.16.4. Molecular Dynamics Analysis. The peptide's root means square deviation (RMSD) indicates how flexible the ligand is within the binding site. The protein structures sampled during the MD simulations were aligned to the MD starting structure, and then the RMSD was calculated for the ligand using *gmx rms*.

To investigate the effect of the allosteric peptides and the occupation of the peptides that bind to the active site, we used the VMD plugin Epock 1.0.5 to evaluate the pocket volume of both active sites of the dimer for 1000 snapshots of the whole MD simulation after fitting the protein to the starting structure.[74] The following simulations were conducted for the second half of the MD simulations: The root-mean-square fluctuation (RMSF) was determined for each peptide with *gmx rmsf* to identify the flexible and rigid areas of the peptide within the protein−peptide complex, and the average minimum distance between specific residues of the protein and peptide was determined using *gmx mindist*.

We used the MM/PBSA method as implemented in gmx_mmpbsa to calculate the binding free energy ΔG_{bind} between the protein and the peptide and to perform alanine scanning.[75] The linear PB equation was solved using the level set function to build the dielectric interface between the solvent and solute.[76] The ionic strength was set to 150 mM. The total nonpolar solvation free energy was modeled as a single term linearly proportional to the solvent-accessible surface area.[77] Here, the binding free energy is defined as

$$\Delta G_{bind} = \langle G_{complex} \rangle - \langle G_{receptor} \rangle - \langle G_{ligand} \rangle$$

with $\langle\rangle$ indicating the average of over 500 snapshots. The free energy for each entity is given as

$$\langle G_x \rangle = \langle E_{bonded} \rangle + \langle E_{nonbonded} \rangle + \langle G_{polar} \rangle + \langle G_{nonpolar} \rangle - \langle TS \rangle$$

where E_{bonded} describes the bonded interactions, $E_{nonbonded}$ indicates the nonbonded, i.e., the Coulomb and Lennard-Jones interactions, and G_{polar} and $G_{nonpolar}$ are the polar and nonpolar contributions to the solvation free energy, respectively. The TS term includes the absolute temperature, T, and the entropy, S.

ΔG_{bind} can also be stated as

$$\Delta G_{bind} = \Delta H - T\Delta S$$

with ΔH the enthalpy of binding and $-T\Delta S$ the conformational entropy after ligand binding. To determine the entropic component, gmx_mmpbsa provides different methods, such as quasi-harmonic (QH) approximation, interaction entropy (IE), or C2 entropy approach. However, these methods were inappropriate for our system, as they either required a large number of snapshots ($\geq 3N$, N = number of complex atoms) or a standard deviation of the interaction energy (sIE) of <3.6 kcal/mol to obtain realistic entropies. Thus, we decided to omit the entropic term, as ΔH is usually sufficient to compare a set of similar ligands by their relative binding free energies.[75] To elucidate the contribution of each peptide residue to the binding free energy, we performed alanine scanning using gmx_mmpbsa. Each residue of the 3CVL and 3CVL-ri peptides (Except Gly and Pro) was substituted by Ala and the enthalpy of binding difference $\Delta\Delta H^{X->A}$ upon alanine mutation was calculated in the following way

$$\Delta\Delta H^{X->A} = \Delta H^{A} - \Delta H^{X}$$

To identify the peptide structures with the most populated configuration or binding pose in the protein−peptide complex, the algorithm of Daura et al. was used as implemented in GROMACS (*gmx cluster*).[78]

The cutoff for clustering the peptide configurations was set to 3.5 Å, and the average structures of the 10 most populated clusters were used for docking against the dimer of the main protease. The binding poses of the peptides in the elongated protein−peptide complex simulations were clustered using a cutoff of 3.0 Å. To avoid biasing of nonbinding flexible areas of the peptide, only those peptide residues with an RMSF of <6 Å were considered for clustering. The three most prominent clusters were then analyzed for interacting residues by generating a contact map.

■ ASSOCIATED CONTENT

Supporting Information

The Supporting Information is available free of charge at https://pubs.acs.org/doi/10.1021/acschembio.2c00735.

Additional experiments and supplementary figures (phage display outcome, inhibitor tests, SPR analysis, HPLC profiles, NMR spectra, and MD analysis) and tables (analysis of peptide sequences selected by phage display and list of amino acids forming the $3CL^{pro}$ substrate-binding site and allosteric site) (PDF)

■ AUTHOR INFORMATION

Corresponding Authors

Mônika A. Coronado − *Institute of Biological Information Processing, Structural Biochemistry (IBI-7), Forschungszentrum Jülich, 52425 Jülich, Germany*; Email: m.coronado@fz-juelich.de

Dieter Willbold − *Institute of Biological Information Processing, Structural Biochemistry (IBI-7), Forschungszentrum Jülich, 52425 Jülich, Germany; Institut für Physikalische Biologie, Heinrich-Heine-Universität Düsseldorf, 40225 Düsseldorf, Germany*; orcid.org/0000-0002-0065-7366; Email: d.willbold@fz-juelich.de

Authors

Raphael J. Eberle − *Institute of Biological Information Processing, Structural Biochemistry (IBI-7), Forschungszentrum Jülich, 52425 Jülich, Germany; Institut für Physikalische Biologie, Heinrich-Heine-Universität Düsseldorf, 40225 Düsseldorf, Germany*; orcid.org/0000-0002-8763-3884

Marc Sevenich − *Institute of Biological Information Processing, Structural Biochemistry (IBI-7), Forschungszentrum Jülich, 52425 Jülich, Germany; Institut für Physikalische Biologie, Heinrich-Heine-Universität Düsseldorf, 40225 Düsseldorf, Germany; Priavoid GmbH, 40225 Düsseldorf, Germany*

Ian Gering − *Institute of Biological Information Processing, Structural Biochemistry (IBI-7), Forschungszentrum Jülich, 52425 Jülich, Germany*

Lara Scharbert − *Institute of Biological Information Processing, Structural Biochemistry (IBI-7), Forschungszentrum Jülich, 52425 Jülich, Germany; Institut für Physikalische Biologie, Heinrich-Heine-Universität Düsseldorf, 40225 Düsseldorf, Germany*

Birgit Strodel − *Institute of Biological Information Processing, Structural Biochemistry (IBI-7), Forschungszentrum Jülich, 52425 Jülich, Germany; Institut für Physikalische Biologie, Heinrich-Heine-Universität Düsseldorf, 40225 Düsseldorf, Germany*; orcid.org/0000-0002-8734-7765

Nils A. Lakomek − *Institute of Biological Information Processing, Structural Biochemistry (IBI-7), Forschungszentrum Jülich, 52425 Jülich, Germany; Institut für Physikalische Biologie, Heinrich-Heine-Universität Düsseldorf, 40225 Düsseldorf, Germany*

Karoline Santur − *Institute of Biological Information Processing, Structural Biochemistry (IBI-7), Forschungszentrum Jülich, 52425 Jülich, Germany; Institut für Physikalische Biologie, Heinrich-Heine-Universität Düsseldorf, 40225 Düsseldorf, Germany*

https://doi.org/10.1021/acschembio.2c00735
ACS Chem. Biol. 2023, 18, 315−330

Jeannine Mohrlüder − *Institute of Biological Information Processing, Structural Biochemistry (IBI-7), Forschungszentrum Jülich, 52425 Jülich, Germany;* orcid.org/0000-0002-9922-2986

Complete contact information is available at: https://pubs.acs.org/10.1021/acschembio.2c00735

Author Contributions

Conceptualization: R.J.E., J.M., and M.A.C.; methodology: R.J.E., M.S., I.G., L.S., B.S., N.A.L., K.B.S., J.M., and M.A.C.; validation: R.J.E., M.S., I.G., L.S., B.S., N.A.L., K.B.S., J.M., and M.A.C.; formal analysis: R.J.E., M.S., I.G., L.S., B.S., N.A.L., K.B.S., J.M., and M.A.C.; investigation: R.J.E. and M.A.C.; resources: B.S. and D.W.; writing—original draft preparation: R.J.E. and M.A.C.; writing—review and editing: R.J.E., M.S., I.G., L.S., B.S., N.A.L., K.B.S., J.M., M.A.C., and D.W. All authors have read and agreed to the published version of the manuscript.

Funding

D.W. received funding from the Deutsche Forschungsgemeinschaft (DFG, German Research Foundation), Project-ID 267205415, SFB 1208. B.S. and L.S. received funding from the VolkswagenStiftung for that project (project number 99761). N.A.L. thanks the German Science Foundation (DFG, grant project number 433700474) for funding as well as support by the project "Virological and immunological determinants of COVID-19 pathogenesis—lessons to get prepared for future pandemics (KA1-Co-02 "COVIPA")", a grant from the Helmholtz Association's Initiative and Networking Fund.

Notes

The authors declare no competing financial interest.

■ ACKNOWLEDGMENTS

Dedicated to Karl-Erich Jaeger for his pioneering contributions in the field of molecular enzyme technology. The authors thank the support of the Institute of Biological Information Processing (IBI-7) Forschungszentrum Jülich, Germany. L.S. and B.S. gratefully acknowledge the computing time granted by the JARA Vergabegremium and provided under project "3cldtp" on the JARA Partition part of the supercomputer JURECA at Forschungszentrum Jülich.

■ REFERENCES

(1) Hu, B.; Guo, H.; Zhou, P.; Shi, Z. L. Characteristics of SARS-CoV-2 and COVID-19. *Nat. Rev. Microbiol.* **2021**, *19*, 141−154.

(2) WHO. *Coronavirus Disease 2019 (COVID-19) Dashboard*; World Health Organization, 2022.

(3) Mathieu, E.; Ritchie, H.; Ortiz-Ospina, E.; Roser, M.; Hasell, J.; Appel, C.; Giattino, C.; Rodés-Guirao, L. A global database of COVID-19 vaccinations. *Nat. Hum. Behav.* **2021**, *5*, 947−953.

(4) Polack, F. P.; Thomas, S. J.; Kitchin, N.; Absalon, J.; Gurtman, A.; Lockhart, S.; Perez, J. L.; Marc, G. P.; Moreira, E. D.; Zerbini, C.; Bailey, R.; Swanson, K. A.; Gruber, W. C.; et al. Safety and efficacy of the BNT162b2 mRNA Covid-19 vaccine. *N. Engl. J. Med.* **2020**, *383*, 2603−2615.

(5) Baden, L. R.; El Sahly, H. M.; Essink, B.; Kotloff, K.; Frey, S.; Novak, R.; Diemert, D.; Spector, S. A.; Rouphael, N.; Creech, C. B.; McGettigan, J.; Khetan, S.; Zaks, T.; et al. Efficacy and safety of the mRNA-1273 SARS-CoV-2 vaccine. *N. Engl. J. Med.* **2021**, *384*, 403−416.

(6) Voysey, M.; Clemens, S. A. C.; Madhi, S. A.; Weckx, L. Y.; Folegatti, P. M.; Aley, P. K.; Bijker, E.; et al. Safety and efficacy of the ChAdOx1 nCoV-19 vaccine (AZD1222) against SARS-CoV-2: an interim analysis of four randomised controlled trials in Brazil, South Africa, and the UK. *Lancet* **2021**, *397*, 99−111.

(7) Livingston, E. H.; Malani, P. N.; Creech, C. B. The Johnson & Johnson Vaccine for COVID-19. *JAMA* **2021**, *325*, 1575.

(8) Owen, D. R.; Allerton, C. M.; Anderson, A. S.; Aschenbrenner, L.; Avery, M.; Berritt, S.; Boras, B.; Cardin, R. D.; Carlo, A.; Coffman, K. J.; Dantonio, A.; et al. An oral SARS-CoV-2 Mpro inhibitor clinical candidate for the treatment of COVID-19. *Science* **2021**, *374*, 1586−1593.

(9) Madsen, L. W. Remdesivir for the Treatment of Covid-19-Final Report. *N. Engl. J. Med.* **2020**, *338*, 1813−1826.

(10) Hosseinzadeh, M. H.; Shamshirian, A.; Ebrahimzadeh, M. A. Dexamethasone Vs. COVID-19: An Experimental Study in Line with the Preliminary Findings of a Large Trial. *Int. J. Clin. Pract.* **2020**, *75*, No. e13943.

(11) Nangaku, M.; Kadowaki, T.; Yotsuyanagi, H.; Ohmagari, N.; Egi, M.; Sasaki, J.; Sakamoto, T.; Hasegawa, Y.; Ogura, T.; Chiba, S.; Node, K.; Suzuki, R.; Yamaguchi, Y.; Murashima, A.; Ikeda, N.; Morishita, E.; Yuzawa, K.; Moriuchi, H.; Hayakawa, S.; Nishi, D.; Irisawa, A.; Miyamoto, T.; Suzuki, H.; Sone, H.; Fujino, Y. The Japanese Medical Science Federation COVID-19 Expert Opinion English Version. *JMA J.* **2021**, *4*, 148−162.

(12) Italian Society of Infectious and Tropical Diseases (SIMIT). *Guidelines for the Teatment and Support Management of Patients with COVID-19 Coronavirus Infection*, 2nd ed.; Italian Society of Infectious and Tropical Diseases (SIMIT): Italy, 2020.

(13) Rambaut, A.; Holmes, E. C.; O'Toole, Á.; Hill, V.; McCrone, J. T.; Ruis, C.; du Plessis, L.; Pybus, O. G. A dynamic nomenclature proposal for SARS-CoV-2 lineages to assist genomic epidemiology. *Nat. Microbiol.* **2020**, *5*, 1403−1407.

(14) Pillaiyar, T.; Manickam, M.; Namasivayam, V.; Hayashi, Y.; Jung, S. H. An overview of Severe Acute Respiratory Syndrome-Coronavirus (SARS-CoV) 3CL protease inhibitors: Peptidomimetics and small molecule chemotherapy. *J. Med. Chem.* **2016**, *59*, 6595−6628.

(15) Jin, Z.; Du, X.; Xu, Y.; Deng, Y.; Liu, M.; Zhao, Y.; Zhang, B.; Li, X.; Zhang, L.; Peng, C.; Duan, Y.; Yu, J.; Wang, L.; Yang, K.; Liu, F.; Jiang, R.; Yang, X.; You, T.; Liu, X.; Yang, X.; Bai, F.; Liu, H.; Liu, X.; Guddat, L. W.; Xu, W.; Xiao, G.; Qin, C.; Shi, Z.; Jiang, H.; Rao, Z.; Yang, H. Structure of Mpro from SARS-CoV-2 and discovery of its inhibitors. *Nature* **2020**, *582*, 289−293.

(16) Rut, W.; Groborz, K.; Zhang, L.; Sun, X.; Zmudzinski, M.; Pawlik, B.; Wang, X.; Jochmans, D.; Neyts, J.; Młynarski, W.; Hilgenfeld, R.; Drag, M. SARS-CoV-2 Mpro inhibitors and activity-based probes for patient-sample imaging. *Nat. Chem. Biol.* **2021**, *17*, 222−228.

(17) Anand, K.; Ziebuhr, J.; Wadhwani, P.; Mesters, J. R.; Hilgenfeld, R. Coronavirus main proteinase (3CLpro) structure: Basis for design of anti-SARS drugs. *Science* **2003**, *300*, 1763−1767.

(18) Ghosh, A. K.; Osswald, H. L.; Prato, G. Recent progress in the development of HIV-1 protease inhibitors for the treatment of HIV/AIDS. *J. Med. Chem.* **2016**, *59*, 5172−5208.

(19) Cannalire, R.; Barreca, M. L.; Manfroni, G.; Cecchetti, V. A journey around the medicinal chemistry of Hepatitis C virus inhibitors targeting NS4B: From target to preclinical drug candidates. *J. Med. Chem.* **2016**, *59*, 16−41.

(20) Craik, D. J.; Fairlie, D. P.; Liras, S.; Price, D. The future of peptide-based drugs. *Chem. Biol. Drug Des.* **2013**, *81*, 136−147.

(21) Mikitsh, J. L.; Chacko, A. M. Pathways for small molecule delivery to the central nervous system across the blood-brain barrier. *Perspect. Med. Chem.* **2014**, *6*, 11−24.

(22) Goodwin, D.; Simerska, P.; Toth, I. Peptides as therapeutics with enhanced bioactivity. *Curr. Med. Chem.* **2012**, *19*, 4451−4461.

(23) Jiang, N.; Leithold, L. H.; Post, J.; Ziehm, T.; Mauler, J.; Gremer, L.; Cremer, M.; Schartmann, E.; Shah, N. J.; Kutzsche, J.; Langen, K. J.; et al. Preclinical pharmacokinetic studies of the tritium labelled D-enantiomeric peptide D3 developed for the treatment of Alzheimer s disease. *PLoS One* **2015**, *10*, No. e0128553.

(24) Leithold, L. H. E.; Jiang, N.; Post, J.; Ziehm, T.; Schartmann, E.; Kutzsche, J.; Shah, N. J.; Breitkreutz, J.; Langen, K. J.; Willuweit, A.; Willbold, D. Pharmacokinetic properties of a novel D-peptide developed to be therapeutically active against toxic β-amyloid oligomers. *Pharm. Res.* **2016**, *33*, 328−336.

(25) Chong, P.; Sia, C.; Tripet, B.; James, O.; Klein, M. Comparative immunological properties of enantiomeric peptides. *Lett. Pept. Sci.* **1996**, *3*, 99−106.
(26) Zhang, T.; Gering, I.; Kutzsche, J.; Nagel-Steger, L.; Willbold, D. Toward the mode of action of the clinical stage all-D-enantiomeric peptide RD2 on Aβ42 aggregation. *ACS Chem. Neurosci.* **2019**, *10*, 4800−4809.
(27) Kutzsche, J.; Jürgens, D.; Willuweit, A.; Adermann, K.; Fuchs, C.; Simons, S.; Windisch, M.; Hümpel, M.; Rossberg, W.; Wolzt, M.; Willbold, D. Safety and pharmacokinetics of the orally available antiprionic compound PRI-002: A single and multiple ascending dose phase I study. *Alzheimer's Dement.* **2020**, *6*, No. e12001.
(28) Schemmert, S.; Camargo, L. C.; Honold, D.; Gering, I.; Kutzsche, J.; Willuweit, A.; Willbold, D. In Vitro and In Vivo Efficacies of the Linear and the Cyclic Version of an All-d-Enantiomeric Peptide Developed for the Treatment of Alzheimer's Disease. *Int. J. Mol. Sci.* **2021**, *22*, 6553.
(29) Valiente, P. A.; Wen, H.; Nim, S.; Lee, J.; Kim, H. J.; Kim, J.; Perez-Riba, A.; Paudel, Y. P.; Hwang, I.; Kim, K. D.; Kim, S.; Kim, P. M. Computational Design of Potent D-Peptide Inhibitors of SARS-CoV-2. *J. Med. Chem.* **2021**, *64*, 14955−14967.
(30) Valiente, P. A.; Nim, S.; Lee, J.; Kim, S.; Kim, P. M. Targeting the Receptor-Binding Motif of SARS-CoV-2 with D-Peptides Mimicking the ACE2 Binding Helix: Lessons for Inhibiting Omicron and Future Variants of Concern. *J. Chem. Inf. Model.* **2022**, *62*, 3618−3626.
(31) Hernández González, J. E.; Eberle, R. J.; Willbold, D.; Coronado, M. A. A computer-aided approach for the discovery of D-peptides as inhibitors of SARS-CoV-2 main protease. *Front. Mol. Biosci.* **2022**, *8*, No. 816166.
(32) Eberle, R. J.; Gering, I.; Tusche, M.; Ostermann, P. N.; Müller, L.; Adams, O.; Schaal, H.; Olivier, D. S.; Amaral, M. S.; Arni, R. K.; Willbold, D.; Coronado, M. A. Design of D-Amino Acids SARS-CoV-2 Main Protease Inhibitors Using the Cationic Peptide from Rattlesnake Venom as a Scaffold. *Pharmaceuticals* **2022**, *15*, 540.
(33) Cardoso, M. H.; Cândido, E. S.; Oshiro, K. G. N.; Rezende, S. B.; Franco, O. L.*Peptide Applications in Biomedicine, Biotechnology and Bioengineering*, Koutsopoulos, S., Ed.; Woodhead Publishing, 2018.
(34) Fischer, P. M. The design, synthesis and application of stereochemical and directional peptide isomers: a critical review. *Curr. Protein Pept. Sci.* **2003**, *4*, 339−356.
(35) Li, C.; Pazgier, M.; Li, J.; Li, C.; Liu, M.; Zou, G.; Li, Z.; Chen, J.; Tarasov, S. G.; Lu, W. Y.; Lu, W. Limitations of peptide retro-inverso isomerisation in molecular mimicry. *J. Biol. Chem.* **2010**, *285*, 19572−19581.
(36) Li, C.; Zhan, C.; Zhao, L.; Chen, X.; Lu, W. Y.; Lu, W. Functional consequences of retro-inverso isomerisation of a miniature protein inhibitor of the p53−MDM2 interaction. *Bioorg. Med. Chem.* **2013**, *21*, 4045−4050.
(37) Cheng, L.; Boland, S.; Scholle, M. D.; Bardiot, D.; Marchand, A.; Chaltin, P.; Blatt, L. M.; Beigelman, L.; Symons, J. A.; Raboisson, P.; Gurard-Levin, Z. A.; Vandyck, K.; Deval, J. Dual inhibition of SARS-CoV-2 and human rhinovirus with protease inhibitors in clinical development. *Antiviral Res.* **2021**, *187*, No. 105020.
(38) Antonopoulou, I.; Sapountzaki, E.; Rova, U.; Christakopoulos, P. Inhibition of the main protease of SARS-CoV-2 (Mpro) by repurposing/designing drug-like substances and utilising nature's toolbox of bioactive compounds. *Comput. Struct. Biotechnol. J.* **2022**, *20*, 1306−1344.
(39) Lockbaum, G. J.; Henes, M.; Lee, J. M.; Timm, J.; Nalivaika, E. A.; Thompson, P. R.; Yilmaz, K. N.; Schiffer, C. A. Pan-3C Protease Inhibitor Rupintrivir Binds SARS-CoV-2 Main Protease in a Unique Binding Mode. *Biochemistry* **2021**, *60*, 2925−2931.
(40) Chen, H.; Wei, P.; Huang, C.; Tan, L.; Liu, Y.; Lai, L. Only one protomer is active in the dimer of SARS 3C-like proteinase. *J. Biol. Chem.* **2006**, *281*, 13894−13898.
(41) Kidera, A.; Moritsugu, K.; Ekimoto, T.; Ikeguchi, M. Allosteric regulation of 3CL protease of SARS-CoV-2 and SARS-CoV observed in the crystal structure ensemble. *J. Mol. Biol.* **2021**, *433*, No. 167324.
(42) Eberle, R. J.; Olivier, D. S.; Amaral, M. S.; Gering, I.; Willbold, D.; Arni, R. K.; Coronado, M. A. The Repurposed Drugs Suramin and Quinacrine Cooperatively Inhibit SARS-CoV-2 3CLpro In Vitro. *Viruses* **2021**, *13*, 873.
(43) Trott, O.; Olson, A. AutoDock Vina: Improving the speed and accuracy of docking with a new scoring function, efficient optimisation, and multithreading. *J. Comput. Chem.* **2010**, *31*, 455−461.
(44) Bojadzic, D.; Alcazar, O.; Chen, J.; Chuang, S. T.; Capcha, J. M. C.; Shehadeh, L. A.; Buchwald, P. Small-Molecule Inhibitors of the Coronavirus Spike: ACE2 Protein−Protein Interaction as Blockers of Viral Attachment and Entry for SARS-CoV-2. *ACS Infect. Dis.* **2021**, *7*, 1519−1534.
(45) Sevenich, M.; Thul, E.; Lakomek, N. A.; Klünemann, T.; Schubert, M.; Bertoglio, F.; van den Heuvel, J.; Petzsch, P.; Mohrlüder, J.; Willbold, D. Phage Display-Derived Compounds Displace hACE2 from Its Complex with SARS-CoV-2 Spike Protein. *Biomedicines* **2022**, *10*, 441.
(46) Singh, E.; Khan, R. J.; Jha, R. K.; Amera, G. M.; Jain, M.; Singh, R. P.; Muthukumaran, J.; Singh, A. K. A comprehensive review on promising antiviral therapeutic candidates identified against main protease from SARS-CoV-2 through various computational methods. *J. Genet. Eng. Biotechnol.* **2020**, *18*, 1−12.
(47) Santur, K.; Reinartz, E.; Lien, Y.; Tusche, M.; Altendorf, T.; Sevenich, M.; Tamgüney, G.; Mohrlüder, J.; Willbold, D. Ligand-Induced Stabilisation of the Native Human Superoxide Dismutase 1. *ACS Chem. Neurosci.* **2021**, *12*, 2520−2528.
(48) Krejci, A.; Hupp, T. R.; Lexa, M.; Vojtesek, B.; Muller, P. Hammock: A hidden Markov model-based peptide clustering algorithm to identify protein-interaction consensus motifs in large datasets. *Bioinformatics* **2016**, *32*, 9−16.
(49) Zhang, L.; Lin, D.; Sun, X.; Curth, U.; Drosten, C.; Sauerhering, L.; Becker, S.; Rox, K.; Hilgenfeld, R. Crystal structure of SARS-CoV-2 main protease provides a basis for design of improved α-ketoamide inhibitors. *Science* **2020**, *368*, 409−412.
(50) Zhang, L.; Lin, D.; Kusov, Y.; Nian, Y.; Ma, Q.; Wang, J.; De Wilde, A.; et al. α-Ketoamides as broad-spectrum inhibitors of coronavirus and enterovirus replication: Structure-based design, synthesis, and activity assessment. *J. Med. Chem.* **2020**, *63*, 4562−4578.
(51) Ma, C.; Sacco, M. D.; Hurst, B.; Townsend, J. A.; Hu, Y.; Szeto, T.; Zhang, X.; Tarbet, B.; Marty, M. T.; Chen, Y.; Wang, J. Bo-ceprevir, GC-376, and calpain inhibitors II, XII inhibit SARS-CoV-2 viral replication by targeting the viral main protease. *Cell Res.* **2020**, *30*, 678−692.
(52) Roy, A.; Lim, L.; Srivastava, S.; Lu, Y.; Song, J. Solution conformations of Zika NS2B-NS3pro and its inhibition by natural products from edible plants. *PLoS One* **2017**, *12*, No. e0180632.
(53) Motulsky, H.; Christopoulos, A.*Fitting Models to Biological Data Using Linear and Nonlinear Regression: A Practical Guide to Curve Fitting*; Oxford University Press, 2004.
(54) Feng, B. Y.; Shoichet, B. K. A detergent-based assay for the detection of promiscuous inhibitors. *Nat. Protoc.* **2006**, *1*, 550−553.
(55) Pervushin, K.; Riek, R.; Wider, G.; Wüthrich, K. Attenuated T2 relaxation by mutual cancellation of dipole-dipole coupling and chemical shift anisotropy indicates an avenue to NMR structures of very large biological macromolecules in solution. *Proc. Natl. Acad. Sci. U.S.A.* **1997**, *94*, 12366−12371.
(56) Skinner, S. P.; Fogh, R. H.; Boucher, W.; Ragan, T. J.; Mureddu, L. G.; Vuister, G. W. CcpNmr AnalysisAssign: a flexible platform for integrated NMR analysis. *J. Biomol. NMR* **2016**, *66*, 111−124.
(57) Elfgen, A.; Santiago-Schübel, B.; Gremer, L.; Kutzsche, J.; Willbold, D. Surprisingly high stability of the Aβ oligomer eliminating all-d-enantiomeric peptide D3 in media simulating the route of orally administered drugs. *Eur. J. Pharm. Sci.* **2017**, *107*, 203−207.
(58) Elfgen, A.; Hupert, M.; Bochinsky, K.; Tusche, M.; González de San Román, M. E.; Gering, I.; Sacchi, S.; Pollegioni, L.; Huesgen, P. F.; Hartmann, R.; Santiago-Schübel, B.; et al. Metabolic resistance of the D-peptide RD2 developed for direct elimination of amyloid-β oligomers. *Sci. Rep.* **2019**, *9*, No. 5715.

(59) Tien, M. Z.; Sydykova, D. K.; Meyer, A. G.; Wilke, C. O. PeptideBuilder: A simple Python library to generate model peptides. *Peer J.* **2013**, *1*, No. e80.
(60) Tang, B.; He, F.; Liu, D.; Fang, M.; Wu, Z.; Xu, D.*AI-Aided Design of Novel Targeted Covalent Inhibitors against SARS-CoV-2*; bioRxiv, 2020.
(61) Goodsell, D.; Morris, G.; Olson, A. Automated docking of flexible ligands: Applications of AutoDock. *J. Mol. Recognit.* **1996**, *9*, 1−5.
(62) Santos-Martins, D.; Forli, S.; Ramos, M.; Olson, A. AutoDock4Zn: An Improved AutoDock Force Field for Small-Molecule Docking to Zinc Metalloproteins. *J. Chem. Inf. Model.* **2014**, *54*, 2371−2379.
(63) Abraham, M. J.; Murtola, T.; Schulz, R.; Pál, S.; Smith, J.; Hess, B.; Lindahl, E. GROMACS: High performance molecular simulations through multi-level parallelism from laptops to supercomputers. *SoftwareX* **2015**, *1−2*, 19−25.
(64) Maier, J. A.; Martinez, C.; Kasavajhala, K.; Wickstrom, L.; Hauser, K. E.; Simmerling, C. ff14sb: Improving the accuracy of protein side chain and backbone parameters from ff99sb. *J. Chem. Theory Comput.* **2015**, *11*, 3696−3713.
(65) Jorgensen, W. L.; Chandrasekhar, J.; Madura, J.; Impey, R.; Klein, M. Comparison of simple potential functions for simulating liquid water. *J. Chem. Phys.* **1983**, *79*, 926−935.
(66) Cauchy, M. A. Méthode généerale pour la ystemson des ystems d' éequa-tions simultanéees. *C. R. Hebd. Seances Acad. Sci.* **1847**, *25*, 536−538.
(67) Bussi, G.; Donadio, D.; Parrinello, M. Canonical sampling through velocity rescaling. *J. Chem. Phys.* **2007**, *126*, No. 014101.
(68) Berendsen, H. J. C.; Postma, J. P. M.; van Gunsteren, W. F.; DiNola, A.; Haak, J. R. Molecular dynamics with coupling to an external bath. *J. Chem. Phys.* **1984**, *81*, 3684−3690.
(69) Nosé, S. Molecular-dynamics method for simulations in the canonical ensemble. *Mol. Phys.* **1984**, *52*, 255−268.
(70) Parrinello, M.; Rahman, A. Polymorphic transitions in single-crystals—a new molecular-dynamics method. *Mol. Phys.* **1981**, *52*, 7182−7190.
(71) Darden, T.; York, D.; Pedersen, L. Particle Mesh Ewald—an N. Log(N) method for ewald sums in large systems. *J. Chem. Phys.* **1993**, *98*, 10089−10092.
(72) Essmann, U.; Perera, L.; Berkowitz, M.; et al. A smooth particle mesh ewald method. *J. Chem. Phys.* **1995**, *103*, 8577−8593.
(73) Hess, B.; Bekker, H.; Berendsen, H.; Fraaije, J. LINCS: A linear constraint solver for molecular simulations. *J. Comput. Chem.* **1997**, *18*, 1463−1472.
(74) Laurent, B.; Chavent, M.; Cragnolini, T.; Dahl, A. C. E.; Pasquali, S.; Derreumaux, P.; Sansom, M. S. P.; Baaden, M. Epock: rapid analysis of protein pocket dynamics. *Bioinformatics.* **2015**, *31*, 1478−1480.
(75) Valdés-Tresanco, M. S.; Valdés-Tresanco, M. E.; Valiente, P. A.; Moreno, E. gmx_MMPBSA: a new tool to perform end-state free energy calculations with GROMACS. *J. Chem. Theory Comput.* **2021**, *17*, 6281−6291.
(76) Wang, J.; Cai, Q.; Xiang, Y.; Luo, R. Reducing grid dependence in finite-difference Poisson−Boltzmann calculations. *J. Chem. Theory Comput.* **2012**, *8*, 2741−2751.
(77) Tan, C.; Tan, Y. H.; Luo, R. Implicit nonpolar solvent models. *J. Phys. Chem. B* **2007**, *111*, 12263−12274.
(78) Daura, X.; Gademann, K.; Jaun, B.; Seebach, D.; van Gunsteren, W.; Mark, A. E. Peptide folding: when simulation meets experiment. *Angew. Chem., Int. Ed.* **1999**, *38*, 236−240.

https://doi.org/10.1021/acschembio.2c00735
ACS Chem. Biol. 2023, 18, 315−330